2014-09-23

High-Performance CMOS Image Sensor and System for Imaging Tissue Hemodynamics

Zhang, Xiao

UNIVERSITY OF CALGARY

High-Performance CMOS Image Sensor and System for Imaging Tissue Hemodynamics

by

Xiao Zhang

A THESIS

SUBMITTED TO THE FACULTY OF GRADUATE STUDIES

IN PARTIAL FULFILMENT OF THE REQUIREMENTS FOR THE

DEGREE OF MASTER OF SCIENCE

GRADUATE PROGRAM IN ELECTRICAL AND COMPUTER ENGINEERING

CALGARY, ALBERTA

SEPTEMBER, 2014

Abstract

Monitoring changes in tissue oxygenation and blood volume is an important aspect of understanding the mechanisms of many diseases and creating corresponding therapeutic interventions. Spectroscopic imaging is adopted in my research to provide a non-contact recording method. Traditionally, such imaging is performed in anesthetized and restrained animals using benchtop instrumentation or miniaturized systems connecting to benchtop instruments through optical fibers or electrical cables, which limits the design and scope of studies. To create a miniaturized imaging system that realizes stand-alone operation on awake and freely-moving rats, I designed and implemented an imaging system, consisting of a miniaturized optical system, a high-performance complementary metal oxide semiconductor (CMOS) image sensor and a storage circuit. The system was electrically and optically characterized and proved to be capable of imaging reflectance changes related to tissue hemodynamics in response to deep brain stimulation (DBS).

Acknowledgements

I wish to express my appreciation to my supervisor Dr. Kartik for his guidance and support throughout my research work. All the contributions in this research owe a great deal to both his ideas and direct assistance. I would also like to thank my co-supervisor, Dr. Yadid-Pecht for her instruction, which gives me a great theoretical foundation on my research.

I would also like thank all my lab mates for their help on research and the great lab environment they offered. I also wish to thank all my friends here for the support and happiness they give to me.

Finally, I would like to profoundly thank my family for their endless love and support. My journey would not have reached here smoothly without their inspirations and encouragements. Warmest appreciation also gives to my girlfriend Jingyan Chen for companying and supporting me all the way.

Dedication

This thesis is dedicated to my family for their endless support, encouragement and love.

Table of Contents

List of Tables

List of Figures and Illustrations

List of Symbols, Abbreviations and Nomenclature

Symbol	Definition
C_{fb}	Feedback capacitance
t_{on}	Time when the burst is high
t_{off}	Time when burst is low during each period
$intensity_{max}$	The maximum intensity, corresponding to the case that power supply is always high and duty cycle is 100%
μ_{dim}	Average signal outputs of pixels in dim region
σ_{dim}	Noise of dim region
i	Pixel number
n_{dim}	Number of pixels in dim region
$p_{f,i}$	Output of the *i-th* pixel
f	Frame number
σ_i	Standard deviation over 400 frames of pixel i
I_0	Emitted light intensity as baseline
I	Reflected intensity detected by the imaging system
λ	Wavelength
$\alpha_{HbO}(\lambda)$	Absorption coefficient of oxyhemoglobin (HbO)
$\alpha_{Hb}(\lambda)$	Absorption coefficient of deoxyhemoglobin (Hb)
ΔC_{HbO}	Changes of concentrations of HbO
ΔC_{Hb}	Changes of concentrations of Hb
$D(\lambda)$	Differential pathlength factor which gives calibration of wavelength λ
$\Delta G(t)$	Change of total blood volume
i_{pd}	Photocurrent
C_{pd}	Photodiode capacitance
V_{th}	Threshold voltage of transistors
Vdd	Power supply
v_{out}	Output voltage
v_{sig}	Signal voltage
v_{samp}	Voltage at n3 and n4
v_{rst}	Reset voltage
Δv	Voltage change
A	Gain of amplifier
V_{OV3}	Overdrive voltage for M3
V_{Tn}	Threshold voltage for nMOS transistor
V_{Tp}	Threshold voltage for pMOS transistor
p	Number of pixels
Q_e	Charge of one electron
I_{light}	Light intensity
h	Planck's constant
c	Speed of light traveling in vacuum
λ	Wavelength
σ_p	Standard deviation of pixel p over 100 frames

Chapter One: Introduction

The eventual goal of this research is to create a high-performance and stand-alone miniaturized imaging system capable of imaging reflectance changes related to tissue hemodynamics, consisting of changes in tissue oxygenation and blood volume, in awake and freely-moving rats without the restriction of optical fibers or electrical cables. This thesis describes fundamental works towards this aim including design of miniaturized optical system and test results, design of high-performance complementary metal–oxide–semiconductor (CMOS) image sensor (CIS) and storage circuit and test results of an imaging system. This chapter lays out motivation of the research and organization of following chapters in the thesis.

1.1 Motivation

Observing changes in tissue hemodynamics is an important approach for learning the mechanisms of many diseases and creating corresponding therapeutic interventions. One important intervention is deep brain stimulation (DBS), which has revolutionized the treatment of movement disorders, such as essential tremor and Parkinson's disease [1]-[3]. However, we only have very limited understanding of the principle of operation of DBS. The understanding is mainly limited by animal testing technology and a trial-and-error approach is the main method used to optimize DBS parameters such as pulse width, frequency and amplitude for new applications. So there is an urgent need to acquire more knowledge on how DBS works.

Spectroscopic imaging is adopted in my research to provide a non-contact approach so it avoids introducing artifacts and enables imaging both morphological (vessel architecture) and functional (perfusion, oxygen content) state of vasculature in tissues.

Traditionally, such imaging is performed in anesthetized and restrained animals using benchtop instrumentation which limits the design and scope of studies. Imaging in awake and freely-moving animals enables studying physiological processes and structures in a close-to-nature state by avoiding extra stress resulting from anesthesia and constraint [4] [5]. Recently there has been a push for miniaturized imaging systems that showed the potential to image the brain in awake and unrestrained animals [6]–[7]. The limitation is mainly the existence of optical fibers or cables that transmit light or electrical signals to and from benchtop components. A miniaturized imaging system that realizes stand-alone operation without fibers or cables would allow biologists to image reflectance changes that can be related to tissue hemodynamics in response to DBS on awake and freely-moving rats.

1.2 Contributions

1) Incorporated an optical system to an existing imaging circuit to make a first generation imaging system and programmed the micro-controller in the system for operation. Also characterized the system and utilized the system for imaging reflectance change in response to DBS.

2) Design all the schematics and part of the layout of a second generation image sensor with the target to improve performances on power consumption, sensitivity, signal-to-noise ratio (SNR) and dynamic range (DR).

3) Based on the above image sensor, I designed a second generation imaging system with a new miniaturized optical system and a storage circuit for writing the data from the image sensor to a microSD card.

4) Characterized the second generation image sensor and system and utilized the system for imaging reflectance change in response to DBS.

1.3 Organization of the thesis

Chapter Two provides a general introduction to DBS and a review of CIS: The focus is on the comparison between CIS and charge-coupled device (CCD) and theories of operation of several types of CIS. Chapter Three describes a miniaturized optical system incorporated in an existing imaging system, the rationale and the results of an experiment to image reflectance changes related to tissue hemodynamics in response to DBS on a rat to test the feasibility of the approach. Chapter Four shows the design of a second generation CIS and the corresponding system. Unlike the previous system which sends outputs to a benchtop instrument, the new system was integrated with a storage circuit based on a microSD card so it avoids the electrical cable sending outputs to a computer. The new system was characterized and tested by imaging reflectance changes related to issue oxygenation in response to DBS in order to check if the system works as expected. Finally, Chapter Five provides a summary and offers some potential research directions.

Chapter Two: Introduction to DBS and CIS

2.1 Introduction to DBS

2.1.1 Background

Animal models are widely used for learning mechanisms of many diseases and creating corresponding therapeutic interventions. One such intervention is DBS. It is basically electrical stimulation in the brain which modulates neural activity [9], [10]. DBS has revolutionized the treatment of movement disorders, such as essential tremor and Parkinson's disease. Recent studies suggest that it also shows the potential to treat psychiatric (depression, obsessive-compulsive disorder), cognitive-neurodegenerative (Alzheimers dementia), and paediatric (Tourettes, epilepsy) disorders and may even relieve chronic pain [12]-[18].

However, we only have very limited understanding of the mechanism of DBS. Our understanding of DBS is mainly limited by animal testing technology and as a result, a trial-and-error approach is the main method used to optimize DBS parameters such as pulse width, frequency and amplitude for new applications despite the widespread recognition of DBS for movement disorders [19]–[22]. So there is a demand to acquire more information on the effects of DBS. Studying tissue hemodynamics in response to DBS contributes to expanding our understanding of the mechanism of DBS.

2.1.2 Methods and requirements to study DBS

DBS modulates neural firing which changes metabolic demands and thus cerebral circulation state. As a result, there are likely hemodynamic changes as well. However, it is unclear whether there are any correlations between electrophysiological and hemodynamic changes [8].

Observing hemodynamic changes in response to DBS offers complementary information on this correlation and thus may improve our understanding of the mechanisms of DBS [11]. There are several methods of recording tissue hemodynamics such as monitoring arterial blood gas (ABG) [3], transcutaneous arterial oxygen tension [4] and optical methods. Compared with other methods, optical approach enables non-contact recording avoiding introducing artifacts and it is capable of recording both the morphological (vessel architecture) and the functional (perfusion, oxygen content) status of vasculature *in vivo* by means of fluorescence, spectroscopy and so on. Specifically, spectroscopic imaging is simple to implement because it doesn't require extra chemical materials.

Traditionally, such imaging is performed in anesthetized and restrained animals using bench top instrumentation which limits the design and scope of studies. Recently there has been a push for miniaturized imaging systems that can potentially image the brain in awake, unrestrained animals [24]–[27]. The main problem of several of these systems is the existence of optical fibers or cables that transmit light or electrical signals to and from bench top component. A miniaturized high-performance imaging system that realizes stand-alone operation without fibers or cables would allow scientists to image reflectance changes that can be mapped to changes in tissue hemodynamics in response to DBS on awake and freely-moving rats.

2.2 Introduction to CIS

The core of a CMOS imaging system is a CIS. A CIS usually consists of a pixel array and periphery circuits such as sample circuits and row and column scanners. The characteristic of a CIS is largely dependent on the design of pixel circuit. The development history of CIS will be

briefly introduced and compared with another dominant image sensor and some typical types of pixel circuit will be described.

2.2.1 Background

The market for solid-state image sensors has been experiencing explosive growth in recent years due to the increasing demands in the fields of mobile imaging, video cameras, surveillance, biomedical imaging and so on [28]. There are mainly two types of solid-state image sensor: charge-coupled device (CCD)-based image sensors and complementary metal oxide semiconductor (CMOS) image sensors. Research about solid-stage image sensors dates from 1960s when passive pixel sensor (PPS) was developed, that is, the CIS without active amplifier in a pixel circuit, but it had a couple of drawbacks especially high noise [29]. Ten years later, CCDs alleviated these problems and offered other advantages such as high sensitivity, small pixel size and so on. As a result, it quickly held sway over the field of image sensors [30].

Another type of CIS, the active pixel sensor (APS), which is an image sensor with an active amplifier in each pixel, was created basically at the same time with CCD [31]. After decades of development, APS have addressed several problems of PPS and offered many advantages over CCDs such as the lower power consumption, higher flexibility and most importantly, the capacity to integrate electronics on-chip thereby reducing components and packaging complexity, size and cost. The advantages are becoming more significant with the development of CMOS technology. Nowadays, CISs are widely used in mobile phones, tablets, DLSRs and so on. They are among the fastest growing and most exciting new segments of the semiconductor industry with tens of millions of parts shipped per year and a compound annual growth rate of over 28% [32].

2.2.2 Classification of CISs

The basic element of a CIS is the pixel circuit. According to whether a pixel contains active amplifier, CISs fall into two categories: passive pixel sensor (PPS) and active pixel sensor (APS). As mentioned before, PPS was the earliest CIS with high noise while APS is the more advanced and common used CIS, which can be sub-classified into a variety of pixel circuits according to the principle of operation, such as a photo gate pixel sensor, photodiode pixel sensor, logarithmic sensor and so forth. CISs can also be classified by technology: standard CMOS process and custom CMOS process. The pixels above are all standard CISs while custom CISs are designed in customized technology and have specific functions: The thin film on ASIC (TFA) image sensor is a good example [33]. The typical CISs are introduced below:

2.2.2.1 PPS

The PPS was first put forward by Weckler at 1967 [34]. The PPS pixel is only made up of a photodiode and a transistor working as a switch as shown in Figure 2.1: The output is connected

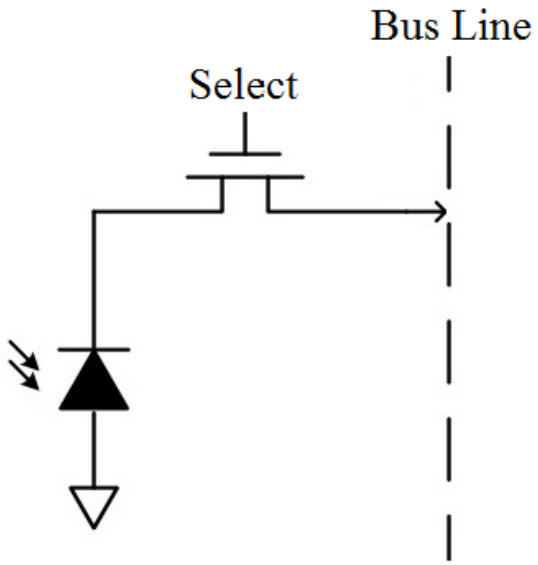

Figure 2.1: Schematic for PPS consisting of a photodiode and a pass transistor as switch

to the cathode of the photodiode through the switch. Since the pixel circuit is very simple, it has very high fill factor (FF), which means the ratio of the size of active area (area that receives light such as a photodiode in pixel) to the total size of a pixel. But the disadvantages are very obvious: The noise is very high [35] and the capacitance of each bus line is too high compared to the photodiode's so the sensitivity becomes low.

2.2.2.2 Photogate APS

Photogate image sensors were first introduced by JPL in 1993 [36]. Basically, they have similar principle of operation to CCDs, which is based on voltage-controlled charge transfer. The schematic is shown in Figure 2.2. Signal charge is integrated under a photogate so light has to penetrate polysilicon so the quantum efficiency (QE) is greatly reduced for some wavelength especially for blue light [36]. QE denotes the ratio of the number of electron-hole-pairs (EHP) generated by photons to the number of incident photons and it is always smaller than 1.

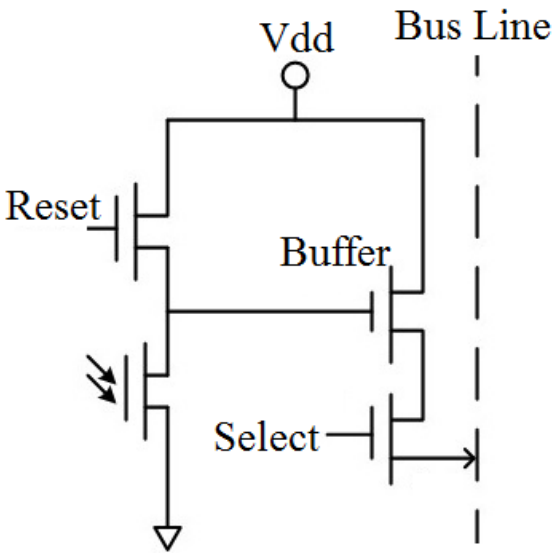

Figure 2.2: Schematic for photogate APS consisting of a photogate structure and three other transistors

2.2.2.3 3-T photodiode APS

3-T photodiode APS is the most basic APS proposed by Noble in 1968 [37]. 3-T here is short for 3-Transistors. As the name implies, the pixel consists of three transistors as shown in Figure 2.3. The photodiode is equivalent to a light-dependent current source in parallel with a capacitor. When reset switch is on, the cathode of the photodiode is connected to power supply, charging the capacitor to high voltage. Then the reset switch turns off and the photocurrent starts to discharge the capacitance. The photocurrent is proportional to light intensity and thus higher light intensity leads to faster decrease of voltage across the capacitor. When select switch turns on, the integration voltage is sent to bus line through a source follower working as a buffer. The reset transistor is usually an nMOS transistor to save space. As a result, the reset voltage is lower than V_{dd} by the threshold voltage, so the dynamic range (DR) are reduced and fixed pattern noise (FPN) as a result of variations of threshold voltages are introduced. Here, the term DR means the ratio of maximum detectable light intensity to the minimum and FPN is a kind of noise that is

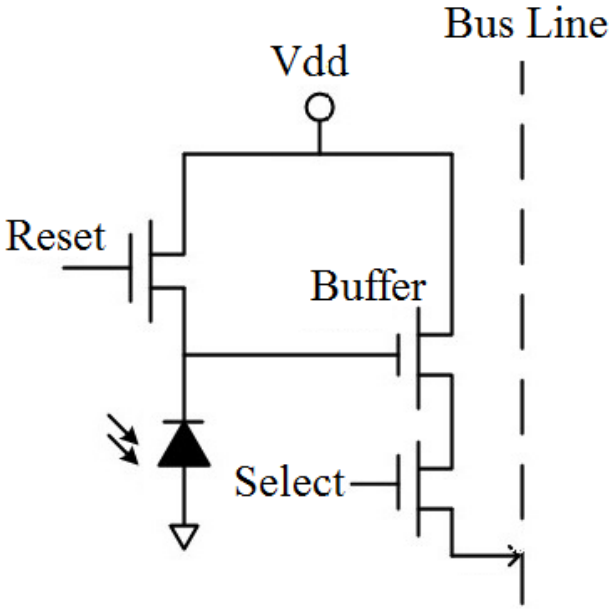

Figure 2.3: Schematic for photodiode 3-T APS consisting of a photodiode, a reset switch, a source follower working as buffer and a select switch

constant for one particular pixel and differs from pixel to pixel. Besides, 3-T APS does not support Correlated Double Sampling (CDS) because reset voltage and integration voltage are not in the same cycle. The term CDS means a sampling circuit that samples the difference between signal voltage and its correlated reset voltage. The correlation here means that the reset voltage and signal voltage needs to be in the same integration cycle. Another type of APS named 4-T APS has been introduced to solve this problem, which will be discussed later in the thesis.

2.2.2.4 4-T photodiode APS

Compared with 3-T APS, 4-T APS has one more transistor: transfer gate (TG), as shown in Figure 2.4 [38]. The function of TG is that it is capable of isolating photodiode and input of the buffer. So the reset voltage is stored in the parasitic capacitance at the input node of buffer. As a result, the reset voltage can be sampled prior to the signal voltage of the same integration cycle. So 4-T transistor is compatible with CDS.

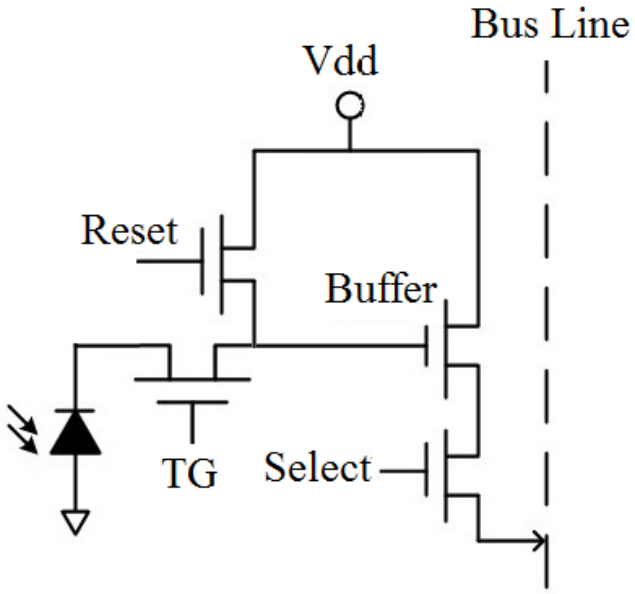

Figure 2.4: Schematic for photodiode 4-T APS consisting of a photodiode, a reset switch, a source follower working as buffer and a select switch and a transfer gate.

2.2.2.5 Snapshot photodiode APS

Snapshot photodiode APS was described by Yadid-Pecht et al. in 1991 [39]. The schematic is shown in Figure 2.5. It is similar with 3-T APS with the exception that it adds a shutter between the cathode of the photodiode and the input of the buffer. The most advantage of this kind of APS is that it allows global shutter, which means that the shutter controls all pixels in an image array simultaneously. Most CIS works in rolling shutter mode which means resetting rows successively and is fine for stationary or low-speed objects. However, rolling shutter mode leads to blur for high-speed imaging and global shutter mode is applied to address this problem.

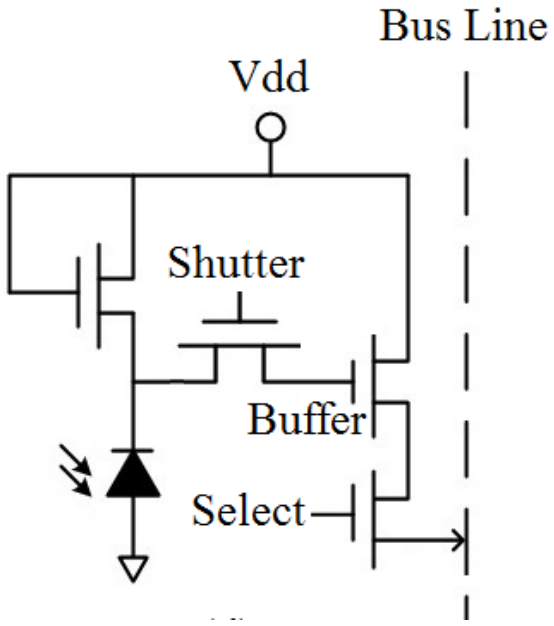

Figure 2.5: Schematic for photodiode Snapshot APS consisting of a photodiode, a bias transistor, a shutter, a source follower working as buffer and a select switch

2.2.2.6 Capacitive transimpedance amplifier (CTIA)-based photodiode APS

CTIA based photodiode APS has been designed to increase sensitivity [40]. The schematic is shown in Figure 2.6. The circuit consists of a photodiode, a CTIA and a reset switch. When reset switch is on, input and output of the amplifier are connected, resulting in a reset voltage. When it

is off, the voltage at the cathode of the photodiode is basically constant because the amplifier has a high gain. As a result, the photocurrent discharges C_{fb} as opposed to photodiode capacitance. So if we set the C_{fb} to be smaller than the photodiode capacitance, we can get high gain from photocurrent to integration voltage. The corresponding drawback is the higher FPN due to the effect of fabrication variation of the smaller capacitance. This pixel is suitable for low light imaging.

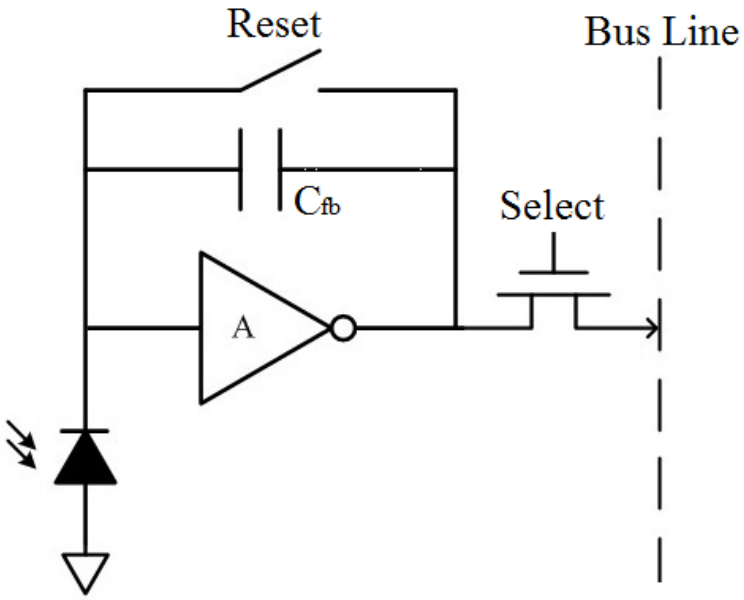

Figure 2.6: Schematic for photodiode CTIA-based APS consisting of a photodiode, an inverting amplifier, a feedback capacitor, a reset switch and a select switch

Spectroscopic imaging depends on multi-wavelength illumination but it is a big challenge for stand-alone miniaturized system to provide powerful illumination due to the limitation of portable power supply such as battery. The high sensitivity feature of CTIA-based APS offers a good solution for this problem. The image sensor described in the thesis is based on CTIA APS and it has several improvements compared with the basic structure shown in Figure 2.6, which will be introduced in Chapter Four.

Chapter Three: Characterization of Miniaturized Optical System and Imaging Reflectance Changes Related to Tissue Hemodynamics in Response to DBS

The eventual goal of the research is to create high-performance and stand-alone miniaturized imaging system capable of imaging reflectance changes related to tissue hemodynamics as a result of DBS. The method adopted in the research is spectroscopic imaging which requires dual-wavelength illumination. The first step towards this goal is to create a miniaturized optical system with two wavelength illumination and integrate it on an imaging system and then test the system to see if it is suitable for spectroscopic imaging.

3.1 Introduction to the miniaturized optical system

The miniaturized optical system consists of a cylinder structure for support, a lens inside for focusing, two LEDs and their current limiting circuits on the bottom layer of the board, as shown in Figure 3.1. The two LEDs emit blue (470nm) and green light (570nm), respectively. Dual-wavelength illuminations enable spectroscopic imaging. The diameter of the cylinder is 18 mm and the height is 11 mm.

The miniaturized imaging system is integrated into an imaging system. The system is essentially a board integrated with the optical system described above, an imager chip, and a microcontroller. The board is shown in Figure 3.1. The square component on the center is the imager package. The cylinder on top of it is miniaturized imaging system. The light intensity of the LED is controlled by pulse width modulation (PWM) function of the controller, so we did not need specific LED drivers, thus saving size and cost. The microcontroller is beneath the imager package to simplify layout and save space. Four potentiometers providing biases are on

the right side. Two rectangle ICs are voltage regulators for analog and digital power supplies, respectively. The imager chip was designed by Murari et al. [41]. It has 132 × 124 capacitive transimpedance amplifier (CTIA)-based pixels with pixel pitch of 20.1 μm fabricated in 0.5 μm CMOS process. It can run as fast as 70 frames per second (fps). This chip is designed to achieve high sensitivity and be capable of imaging in low light environment. For the wavelength of 450 nm it can detect light intensity as low as 4 nW/cm^2 or 520 photons at the speed of 70 fps [41].

While the chip has been characterized previously [41], this chapter shows a more comprehensive characterization mainly for the optical system.

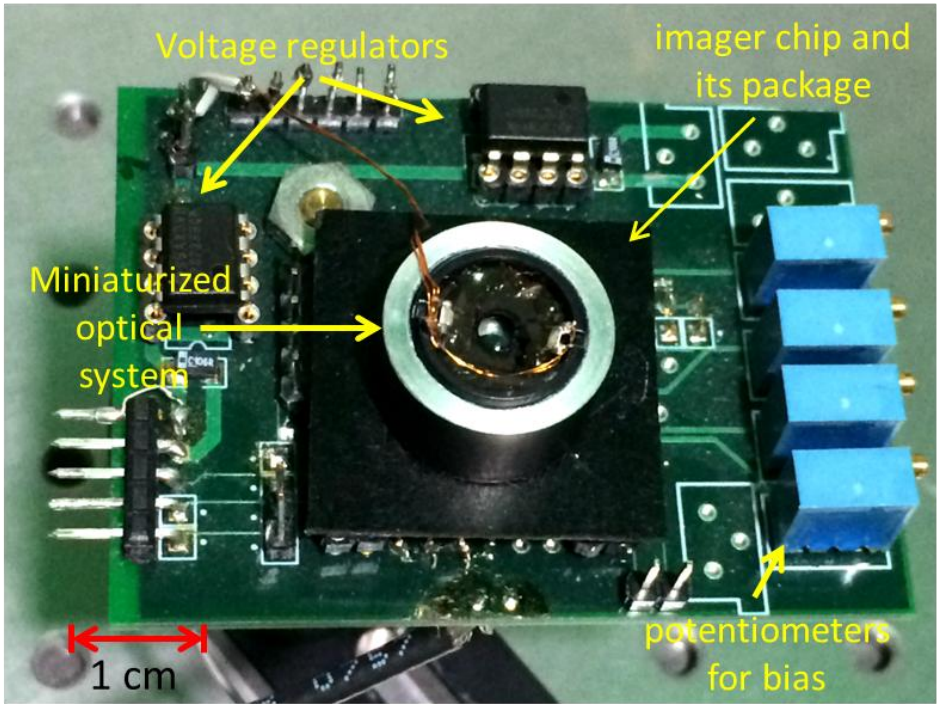

Figure 3.1: Picture of the CMOS imaging system. The biggest square component on the center is the imager package. The miniaturized imaging system consists of the cylinder on top the imager package, a lens inside the cylinder and two LEDS on top of the cylinder and connecting wires. Four potentiometers providing biases are on the right. Two rectangle ICs are voltage regulators for analog and digital power supplies, respectively.

3.2 Characterization of the imaging system

3.2.1 Illumination spatial uniformity

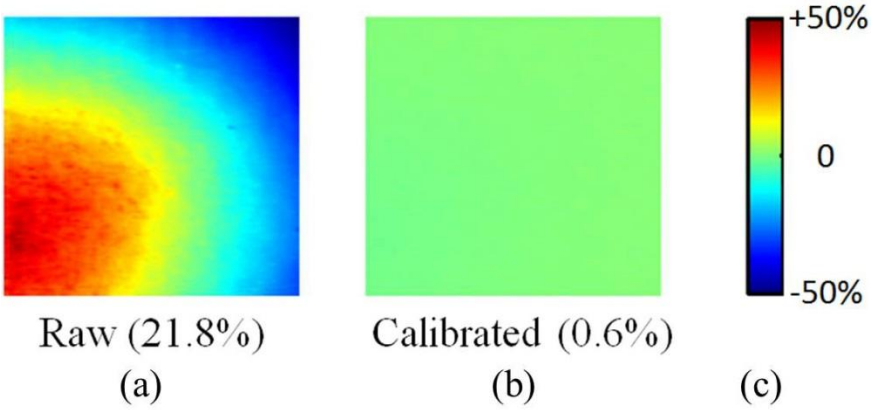

Figure 3.2: (a) Raw image showing illumination non-uniformity measured as relative deviation from the mean of the entire image of a featureless flat surface taken under blue light illumination, (b) two-point calibrated image of the raw image and (c) color bar.

To characterize spatial uniformity of illumination, a flat featureless surface was used as the target. The raw image taken under blue light is shown in Figure 3.2 (a). The value of each pixel in the image is the relative deviation of the output of each pixel compared with the spatial average of the entire pixel array. In other words, the image shows spatial relative nonuniformity rather than an actual image. According to the colorbar shown in Figure 3.2 (c), green region means good uniformity while red or blue indicates more non-uniformity. The raw image has a ratio of standard deviation to the spatial average of 21.8%, which is mainly a result of asymmetric light source. Then two-point calibration [42] was utilized to correct the image and the result is shown in Figure 3.2 (b). Visually it is much more uniform, which is confirmed by its ratio of standard deviation to the mean of 0.6%. We also corrected non-uniformity under green illumination and the ratio was corrected from 22.6% to 0.5%. It seems that poor illumination

spatial uniformity performance is not a problem because it can be calibrated. However, the calibration requires a brighter image and darker image than the raw image so the intensity of raw image cannot be very low or high, which leads to the decrease of DR.

3.2.2 PWM control of illumination intensity

Illumination intensity affects some important performance parameters such as noise ratio (SNR) and contrast to noise ratio (CNR) directly. Illumination intensity control is important for the system to image targets of different reflectance at variable exposure times. We utilized PWM function of the microcontroller to realize linear intensity control of the two LEDs. In this implementation, LEDs are controlled by a burst and the duty cycle of the burst can be adjusted by the microcontroller. If the frequency of the burst is set to be fast enough, the light intensity of the LED is linearly related to the duty cycle:

$$intensity = \frac{t_{on}}{t_{on} + t_{off}} \cdot intensity_{max} = (duty\ cycle) \cdot intensity_{max} \qquad (3.1)$$

where t_{on} denotes the time when the burst is high, t_{off} represents the time when burst is low during each period and $intensity_{max}$ denotes the maximum intensity corresponding to the case that power supply is always high and duty cycle is 100%.

Figure 3.3 illustrates the light intensity measured by an optical power meter with PWM duty cycle varied from 10% to 100% under two different light wavelengths: 470 nm and 570 nm, respectively. The linear relationship is clearly shown in the diagram. With the help of PWM, we can realize linear control of light intensity without specific LED drivers, simplifying the system and saving space, which is an important step towards miniaturized imaging system.

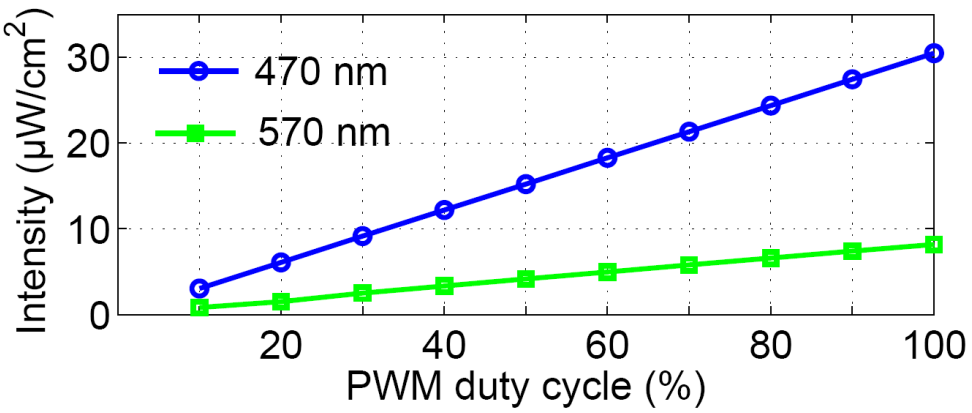

Figure 3.3: Light intensity at two wavelength controlled linearly by PWM duty cycle from 10% to 100%

3.2.3 Resolution

To characterize the resolution of the system, a 1951 USAF resolution chart shown in Figure 3.4 (a) was used and images were taken of the 2.5mm×2.5mm region surrounded by a red square. The vertical red line added to the figure crosses 5 elements and each element consists of three horizontal and vertical black lines. The distance between the three lines decreases from the element on the top to the one on the bottom. So ideally, we can get the intensity diagram shown in Figure 3.4 (b): For each element labeled from 2 to 6, three valleys represent three dark lines in each element because the intensity of dark regions is low while the two peaks in between show the spaces between the lines. As can be seen, the peaks narrow down from element 2 to 6 indicating that the distance between the bars is decreasing. Similarly, we analyzed the intensity along the line in the real image taken by the system as shown in Figure 3.4 (b) and the result is shown Figure 3.4 (d). From element 2 to element 5, we can clearly distinguish two peaks from three valleys while for element 6, it is obscure. This result indicates a resolution of 25 line pairs/mm or 20 μm, which is limited by the pixel size. In other words, the optical module of the system does not degrade image quality in terms of resolution.

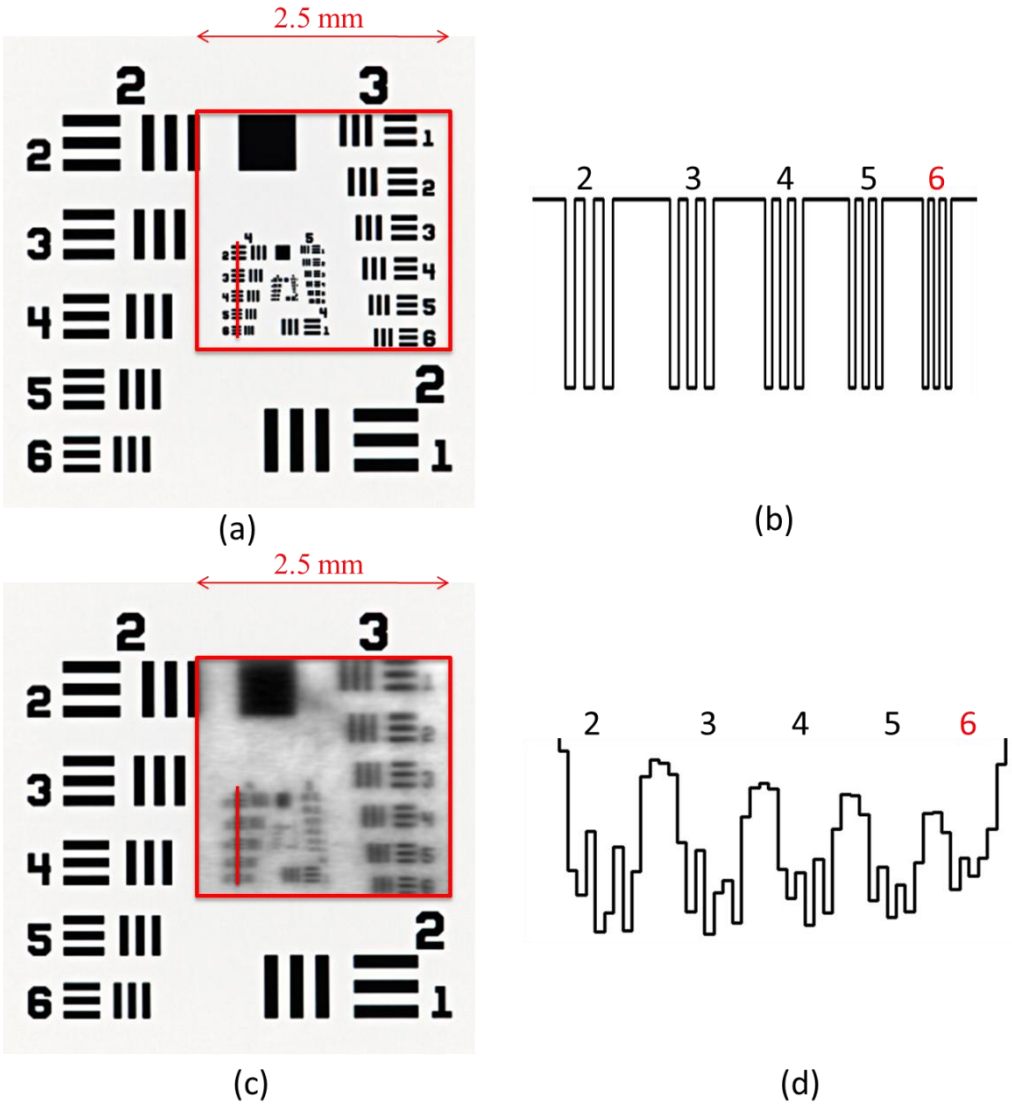

Figure 3.4: (a) 1951 USAF resolution chart, 2.5mm×2.5mm red square indicates the region to be imaged and the intensity along the red vertical is the ideal situation, (b) the ideal intensity along the red vertical line, (c) 1951 USAF resolution chart with the actual image taken by the system in the red square outline and the intensity along the red vertical short line is to be analyzed as actual case and (d) the actual intensity showing resolution limitation.

3.2.4 SNR and CNR

To characterize SNR and CNR under certain illumination, we used a target with black and white bands to realize high contrast. The image of the target is shown in Figure 3.5 (a). We

characterized the SNR for bright and dim regions separately. For each region, the signal was calculated as the average of all pixels in this region over 400 frames. To acquire the noise information, we calculated the standard deviation of each pixel over 400 frames and added standard deviations of all pixels in the region quadratically. Thus the SNR for dim region is given by

$$\mathrm{SNR_{dim}} = \frac{\mu_{\mathrm{dim}}}{\sigma_{\mathrm{dim}}} = \frac{\sum_{i=1}^{n_{\mathrm{dim}}} \sum_{f=1}^{400} p_{f,i}}{\sqrt{\frac{\sum_{i=1}^{n_{\mathrm{dim}}} {\sigma_i}^2}{n_{\mathrm{dim}}}}} \tag{3.2}$$

where μ_{dim} denotes the signal and σ_{dim} represents the noise of dim region, f represents frame and i denotes pixel number. Here $p_{f,i}$ denotes the output of the *i-th* pixel at the *f-th* frame and there are n_{dim} pixels in dim region in each frame. For example, $p_{3,5}$ is the 3rd pixel in the *5-th* frame. σ_i denotes the standard deviation over 400 frames of the *i-th* pixel. There is a different SNR at different light intensities and SNR for bright region can be calculated similarly. Light intensity is varied by the PWM control and the SNR vs. light intensity of both the bright and dim regions is plotted in Figure 3.5 (b): Bright region has higher SNR compared with dim region under the same illumination and the SNR of both dim and bright region increases with illumination intensity linearly. The result is consistent with expectation.

CNR is similar to SNR except that the numerator is the difference between the mean of bright and dim region and the noise takes all pixels in the image into account, which is given by

$$\mathrm{CNR} = \frac{\mu_{\mathrm{bright}} - \mu_{\mathrm{dim}}}{\sqrt{\frac{\sum_{i=1}^{n_{\mathrm{total}}} {\sigma_i}^2}{n_{\mathrm{total}}}}} = \frac{\mu_{\mathrm{bright}} - \mu_{\mathrm{dim}}}{\sqrt{{\sigma_{\mathrm{bright}}}^2 . \frac{n_{\mathrm{bright}}}{n_{\mathrm{total}}} + {\sigma_{\mathrm{dim}}}^2 . \frac{n_{\mathrm{dim}}}{n_{\mathrm{total}}}}} \tag{3.3}$$

The CNR increase linearly with illumination intensity as expected, showing the ability to distinguish between brighter and darker regions.

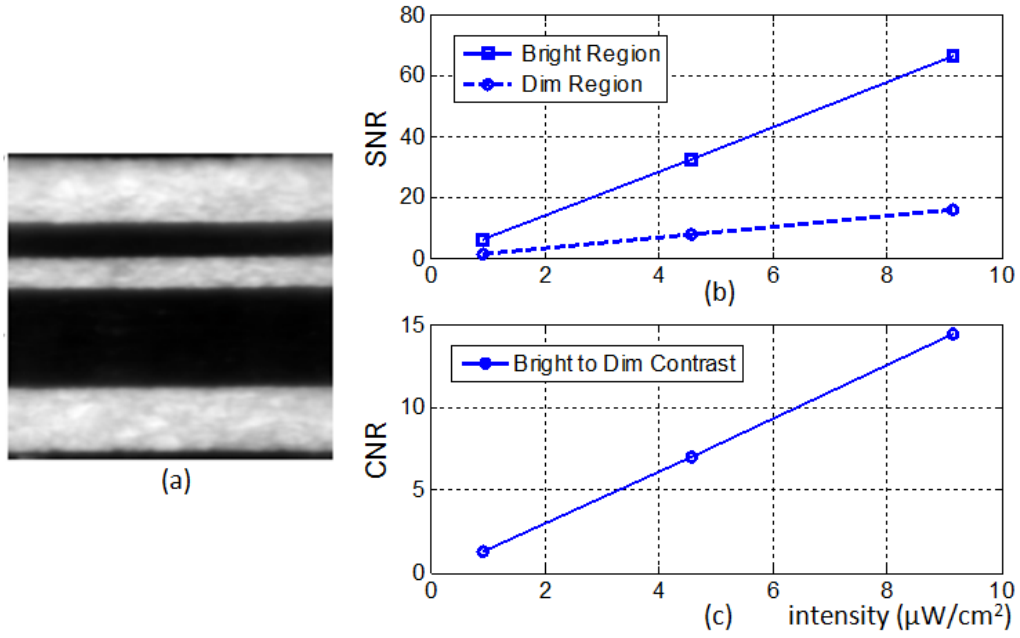

Figure 3.5: (a) high contrast target with dim and bright bands for SNR and CNR test, (b) SNR vs. light intensity for bright region and dim region under blue illumination and (c) CNR vs. light intensity under blue illumination.

The characterization of the system on spatial uniformity, PWM control, resolution, SNR and CNR has been described in this section. The next section shows the rationale, procedure and results of an experiment imaging reflectance changes that are related to tissue hemodynamics.

3.3 Spectroscopic imaging of hemodynamic changes due to DBS

3.3.1 Theory

In visible spectrum, the hemoglobin in blood is the main source that absorbs light and creates intrinsic contrast in brain tissues [43]-[47]. Under this precondition, spectroscopic imaging is capable of recording changes in the reflectance which can be related to changes in tissue hemodynamics with blue and green light according to modified Beer-Lambert law. Beer-Lambert law describes the relationship between attenuation spectrum to the path length and the

absorption coefficient of the medium through which the light is traveling while the modified Beer-Lambert law takes scattering losses, path-length changes due to multiple scattering in the material through which light is travelling into account so it can be applied to highly scattering material such as tissues [48] [49]. For hemodynamic imaging, the modified Beer-Lambert law is given by [47] [48]

$$\log_{10}\left(\frac{I_0}{I(t)}\right) = (\alpha_{HbO}(\lambda)\Delta C_{HbO} + \alpha_{Hb}(\lambda)\Delta C_{Hb})D(\lambda) + \Delta G(t) \tag{3.4}$$

where I_0 denotes initial light intensity as a baseline while I(t) denotes the reflected intensity detected by the imaging system at time t. $\alpha_{HbO}(\lambda)$ and $\alpha_{Hb}(\lambda)$ represents the absorption coefficients of oxy-hemoglobin (HbO) and deoxy-hemoglobin (Hb) at wavelength of λ, respectively, from baseline to time t. The Hb here refers to the hemoglobin that does not carry oxygen while the HbO denotes the hemoglobin carrying oxygen. ΔC_{HbO} and ΔC_{Hb} denote the changes of concentration of HbO and Hb, respectively. Since HbO and Hb shift with each other, we have $\Delta C_{HbO} = -\Delta C_{Hb}$. Here $\Delta G(t)$ is the change of a geometric factor associated with scattering losses at time t and it depends on blood volume in the region of interest (ROI): If the blood volume increases from the baseline, there are more scattering losses resulting a larger G(t) . As for $D(\lambda)$, it is the differential pathlength factor which provides calibration based on the fact that different wavelength travels through different pathlength in tissues. In this equation, $D(\lambda)$, $\alpha_{HbO}(\lambda)$ and $\alpha_{Hb}(\lambda)$ are known if λ is determined, and I_0 and I(t) are reflected intensities that can be measured by imaging system. ΔG, ΔC_{HbO} and ΔC_{Hb} are the unknowns. Spectroscopic imaging with multiple wavelengths results in multiple equations which can be used to solve for the unknowns.

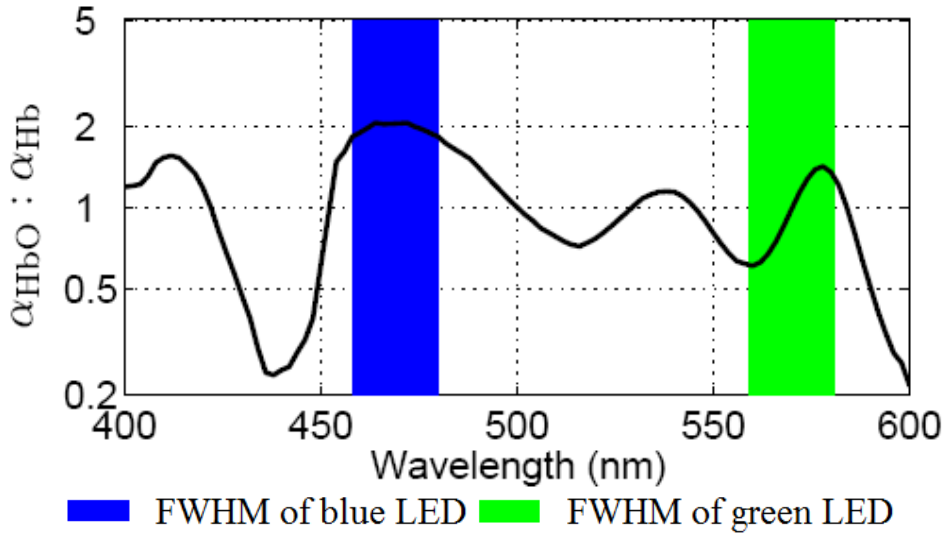

Figure 3.6: Y axis shows the ratio of α_{HbO} to α_{Hb}. Blue band indicates the FWHM wavelength of blue light centered at 470nm while green band shows the FWHM wavelength of green light centered at 570 nm. Within this band, the ratio is almost two, indicating that α_{HbO} is nearly twice of α_{Hb} under illumination of blue light. Similarly, green band shows the FWHM wavelength of the green light centered at 570 nm, and in this band, the average ratio is 1, implying that α_{HbO} equals to α_{Hb} under illumination of green light.

Figure 3.6 shows the ratio of α_{HbO} to α_{Hb} for different wavelengths. The green band shows the full width at half maximum (FWHM) wavelength of the green light centered at 570 nm, and in this band, the average ratio is 1, implying that α_{HbO} equals to α_{Hb} under illumination of green light. Then the modified Beer-Lambert law is given by

$$\lg\left(\frac{I_0}{I(t)}\right) = \alpha_{HbO}(570nm)(\Delta C_{HbO} + \Delta C_{Hb})D(570nm) + \Delta G(t) = \Delta G(t) \qquad (3.5)$$

It means that reflected intensity only varies with $\Delta G(t)$. In other words, the change of reflectance depends on the change of total blood volume and it is not affected by the concentration of oxygen.

The blue band indicates the FWHM wavelength of blue light centered at 470nm. Within this band, the ratio is almost two, indicating that α_{HbO} is nearly twice of α_{Hb} under illumination of

blue light. Similarly, according to modified Beer-Lambert law:

$$\lg\left(\frac{I_0}{I(t)}\right) = \alpha_{Hb}(470nm)(2\Delta C_{HbO} + \Delta C_{Hb})D(470nm) + \Delta G(t) = \alpha_{Hb}(470nm)\Delta C_{HbO}D(470nm) + \Delta G(t) \quad (3.6)$$

It is shown that for blue light, the change of reflected intensity depends both on the change of blood volume and the change of HbO.

Based on this, we imaged tissues alternately under blue and green light illumination before, during and after DBS. The change of reflected light under green light indicates the change of blood volume in the imaging area. As for the result under blue light, it can be either caused by the change of oxygenation or blood volume, so it needs to be analyzed in combination of green light.

3.3.2 Experimental procedure

We performed a craniotomy on the skull to create a 5 mm × 5 mm window centered over the primary motor cortex of an anesthetized female Sprague-Dawley rat for imaging and drilled another hole to put in a DBS electrode into the thalamus which has excitatory projections to the primary motor cortex. The experimental setup is shown in Figure 3.7 (a). The imaging system was positioned right above the primary motor cortex of the rat. Body temperature was maintained at 37 Celsius and the stimulation parameters are shown in Table 3.1.

The experiment process is shown in Figure 3.8. We first gave a start trigger, the imaging system started to take images immediately after the start trigger at a speed of 15 fps under alternative illumination of blue light and green light. The two lights alternated every 1 second. After a delay of 10 s, the stimulator started to work and the stimulation lasted for 10 s. The imager stopped after 60 s. Then we processed and analyzed the data.

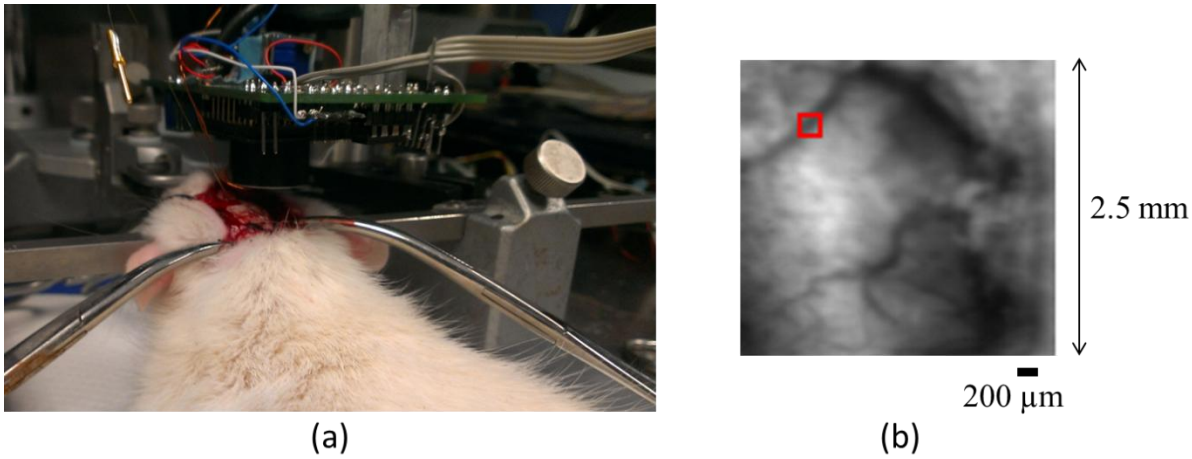

Figure 3.7: (a) Experiment setup: The rat is anesthetized and positioned in in a stereotaxic frame and the imaging system is right above the primary moto cortex of the rat and (b) a typical image of primary motor cortex taken by the system and the red square outline it our ROI to be analyzed.

Table 3.1: DBS parameters including stimulation frequency, pulse width, current amplitude and duration of simulation.

Frequency	150 Hz
Pulsewidth	200 µs
Duration	10 s
Amplitude	600 µA

3.3.3 Results analysis

A typical image taken by the imaging system is shown in Figure 3.7 (b). The 200 µm × 200 µm region surrounded by the red square is the ROI for subsequent analysis. In every second, the system acquired 15 frames and the spatial average of the ROI of each frame was calculated, resulting in 15 average reflected intensities. Then we calculated the temporal average and standard deviation of the 15 intensities and as a result, we had 1 mean and 1 standard deviation every second. The mean shows average reflected intensity of this second while standard deviation contains temporal noise and intensity change information of this second.

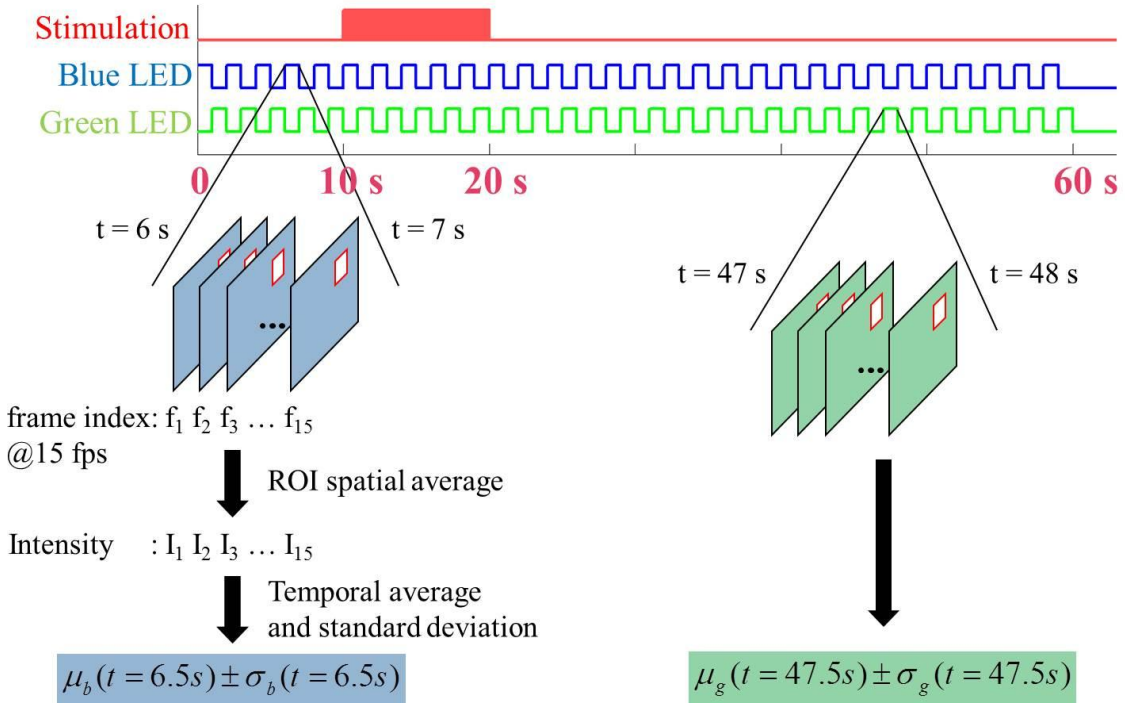

Figure 3.8: Waveforms show that simulation is from 10 s to 20s. Pulses for blue and green LEDs show working cycles of each LED and each working cycle is 1 s. 15 frames were acquired during blue light cycle from 6 s and 7 s are shown as an example. The ROI surrounded by the square outline of every frame was averaged to show the intensity of each ROI. Then the mean and standard deviation of the 15 average intensities were calculated to represent the average intensity and variation for this 1-s cycle. The same process goes with every cycle for both blue and green light.

Then we used the data in the first ten seconds (before stimulation began) to normalize mean and standard deviation of each second and plotted the change in reflectance, denoted by Δ reflectance, in the form of normalized mean ± standard deviation as shown in Figure 3.9. Thus, Δ reflectance means the relative change compared with average reflectance in the first ten seconds. If the reflected intensity does not change, then Δ reflectance stays at zero.

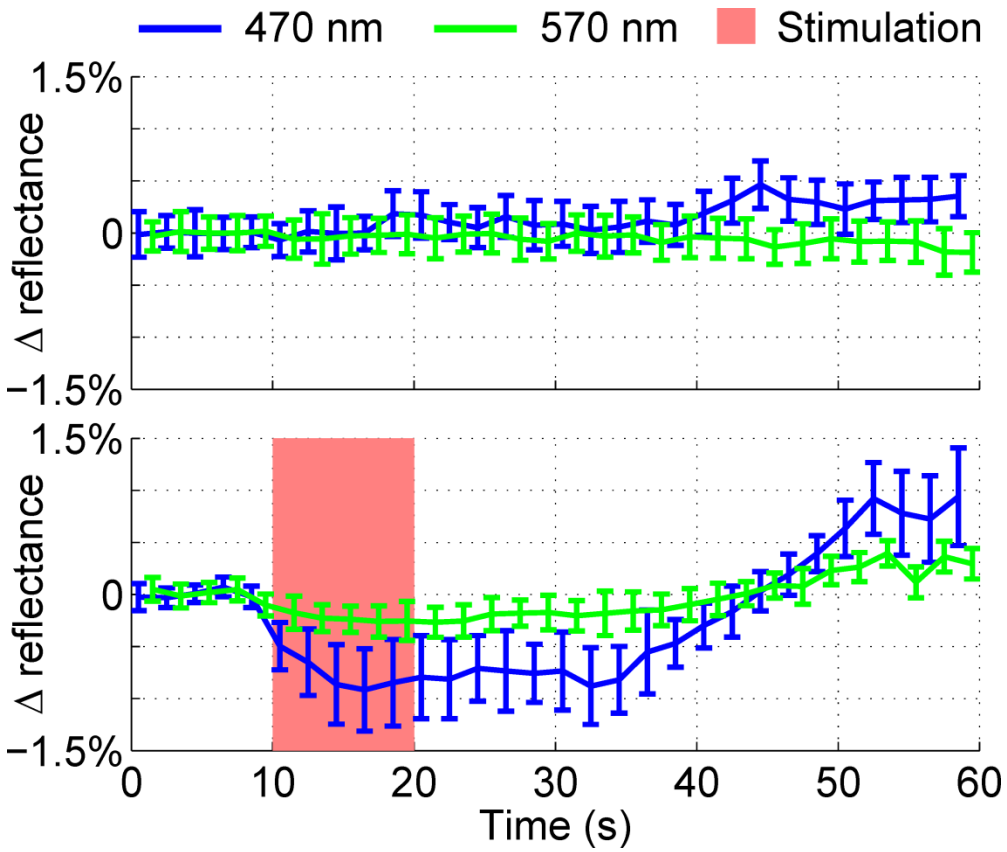

Figure 3.9: The Δ reflectance is plotted in the form of normalized mean ± standard deviation of the data without (upper plot) and with DBS (lower plot). The data of the first second were used to normalize mean and standard deviation to show relative change of reflectance. The maximum reduction for green illumination is about 0.3% and about 0.8% for blue illumination. The reflectance still stays for some time after the cease of stimulation and then rises up.

The upper plot in Figure 3.9 shows the condition without stimulation in which the Δ reflectance is around 0 and the lower one shows the result with stimulation, the reflectance starts to decrease once the stimulation starts. For green light, the reflectance decreases by about 0.3% about 4 seconds after the onset of DBS, indicating more scattering losses and thus the increase of blood volume in the area selected. As for blue light, the reflectance decreases to the lowest level about 5 seconds after the onset of DBS. The maximum change of reflectance is about 0.8%, indicating changes in both the blood volume and the tissue oxygenation. The reflectance then

starts to increase after a delay when the DBS ends and increases to a higher level compared to the initial state. Longer imaging time will be needed to observe the status after that, but it is beyond the scope of this thesis. Though further research is required for a more conclusive statement, the result indicates observable reduction of reflectance and thus the increase of both blood volume and oxygen concentration as a result of the stimulation detected by the system.

In next chapter, a modified miniaturized optical system with smaller size and better illumination performance will be introduced. What's more, a high-performance image sensor will be described and an imaging system based on them will be used to do the test again. The new system will avoid the used of cables sending outputs to benchtop instrument and it has portable storage circuit based on microSD card. The results of the test will be stored in the microSD card and analyzed in computer to get the result.

Chapter Four: Second Generation CIS and System for Imaging Reflectance Changes Related to Tissue Hemodynamics in Response to DBS

To improve the performance of the imager described in Chapter Three, I designed a second generation imager with higher sensitivity, better SNR and dynamic range, lower power consumption and better resolution. I also designed a second generation imaging system with the new imager, a second generation miniaturized optical system and a data storage circuit based on microSD card so the system can work in a stand-alone fashion, without needing to connect to a computer to store data. We characterized the system and tested it by imaging reflectance changes related to hemodynamic changes as a result of DBS, storing the images in a microSD card and subsequently analyzing the data.

4.1 Imager design

4.1.1 Overview

The second generation imager is a based on the previous one. Compared with previous generation, its pixel size is reduced because of the smaller transistor size due to a different technology and symmetric pixel layout which enables the sharing of one ground bus by two columns of pixels. All amplifiers were adjusted repeatedly to achieve as good gain and bandwidth performance as possible at small size and low power consumption. What's more, column-level single-slope ADCs were designed and integrated in the chip. The new generation imager was expected to achieve higher SNR, DR and sensitivity and lower power consumption than previous one. The block diagram of the imager chip is shown in Figure 4.1. The pixel array consists of 144×144 pixels, 144 column-parallel sample/hold (S/H) circuits, row and column

scanners, 144 column-parallel analog-to-digital convertors (ADC) and output buffers. The basic principle of operation is that under the control of an off-chip processor such as microcontroller, row scanner selects rows one by one. Once a row is selected, S/H circuits samples the voltage and holds it to be shifted out consecutively through a buffer or be converted to digital outputs. Then this row is reset and starts a new integration cycle and next row is selected and follows the same process. This fashion is called rolling shutter mode.

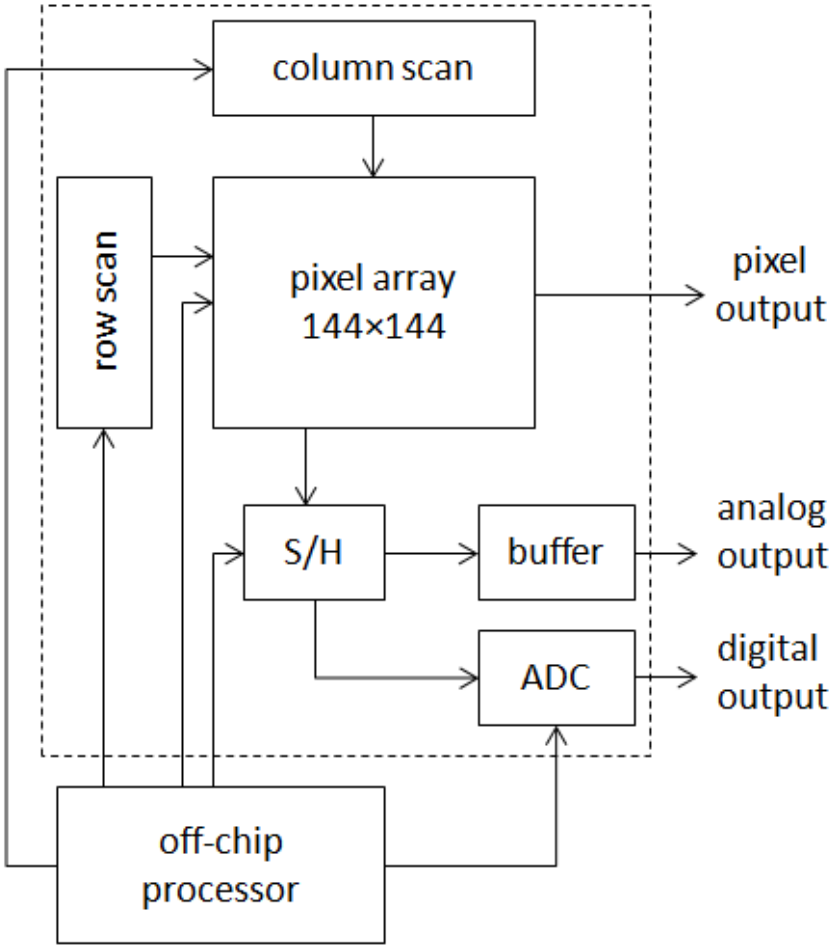

Figure 4.1: Block diagram of the imager consisting of a pixel array, row and column scanners, S/H circuits, ADCs and buffers.

4.1.2 Pixel Circuit

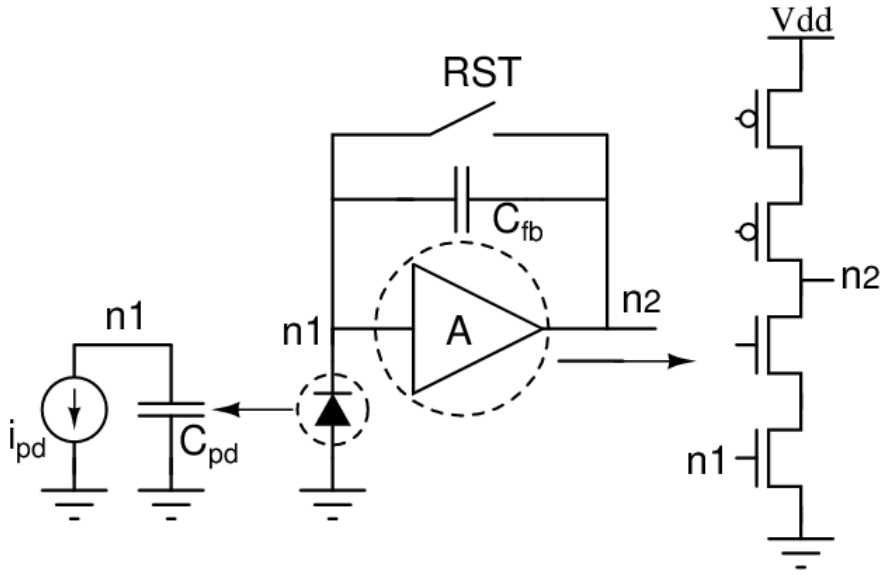

Figure 4.2: Schematic of the CTIA-based pixel circuit

The pixel circuit is shown in Figure 4.2. It is based on CTIA APS. Compared with the CTIA pixel circuit which was first introduced by Boyd et al. and some other image sensors based on CTIA, the CTIA pixel circuit we adopted used a cascode amplifier instead of an operational amplifier and the pMOS transistors of the amplifier are shared by a column to save space and increase FF [40] [58]. It consists of a photodiode, a CTIA and a reset switch denoted as RST. The photodiode is equivalent to a current source i_{pd} in parallel with capacitance C_{pd}. The amplifier is an inverting cascode amplifier with the gain of –A and A is a positive value. When reset switch is on, input and output of the amplifier are connected, resulting in a reset voltage at the two nodes. When reset switch is off, input and output of the amplifier are connected through C_{fb}. According to Miller effect, C_{fb} is equivalent to two capacitors at bith input and output terminals of the amplifier respectively as shown in Figure 4.3. After time t, the voltage change at input node n1 is

$$\Delta v_{in} = -\frac{\int i_{pd} dt}{C_{pd}+(A+1)C_{fb}} \tag{4.1}$$

So the output voltage change is described as

$$\Delta v_{out} = -A\Delta v_{in} = \frac{A\int i_{pd} dt}{C_{pd}+(A+1)C_{fb}} \tag{4.2}$$

If the gain is high enough to satisfy $(A+1)C_{fb} \gg C_{pd}$ and $A \gg 1$, then

$$\Delta v_{out} \approx \frac{A\int i_{pd} dt}{(A+1)C_{fb}} \approx \frac{\int i_{pd} dt}{C_{fb}} \tag{4.3}$$

The output voltage is the integration of photocurrent over time t divided by C_{fb}. Compared with conventional 3-T CISs which follow

$$\Delta v_{out} \approx \frac{\int i_{pd} dt}{C_{pd}} \tag{4.4}$$

if C_{fb} is half of C_{pd}, the output of CTIA pixel doubles. This is the basis to achieve high sensitivity for CTIA pixel. In our circuit, C_{fb} was designed to be 2.1 fF, which is much smaller than conventional C_{pd} which is typically more than one order of magnitude larger.

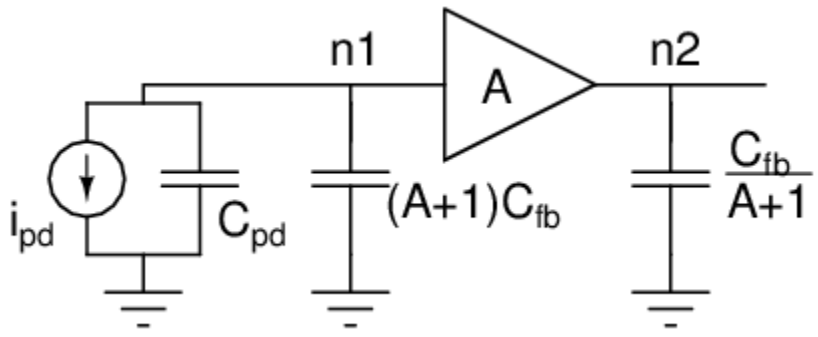

Figure 4.3: Equivalent pixel circuit based on Miller effect

The CTIA consists of a cascode amplifier and a feedback capacitor C_{fb}, which is shown in Figure 4.4 (a). The cascode amplifier is made up of two nMOS transistors: M1 (1.4 μm/ 0.7 μm)

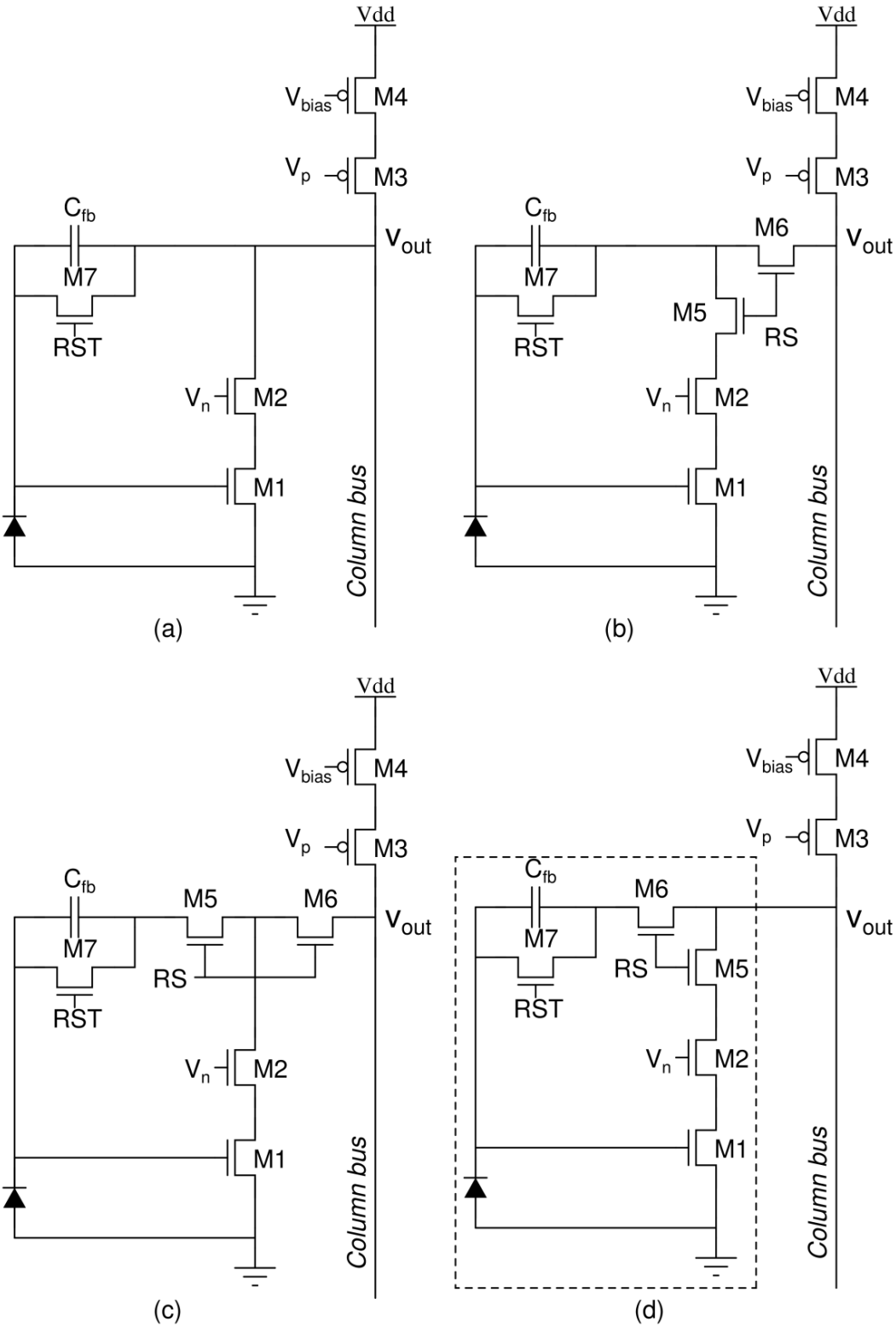

Figure 4.4: Schematic of CTIA based pixel circuit. Two pMOS transistors of CTIA are shared by a whole column. The pixel circuit is indicated by the rectangle with dashed outline.

and M2 (0.7 μm/ 2.1 μm) and two pMOS transistors: M3 (1.4 μm/ 1.4 μm) and M4 (1.4 μm/ 1.4μm). M2 and M3 are utilized to increase the gain. The gain, gain-bandwidth (GBW) and bias current of the amplifier are shown in Table 4.1. Transistor M7 (0.4 μm/ 0.35 μm) works as a reset switch. For analog transistors, the minimum length is set to be 0.7 μm, that is, twice of the smallest length allowed in 0.35-μm technology as a result of trade-off between small size and small fabrication variation. The ratio of width to length (W/L) of M4 is only 1 so the bias current is low for power-saving consideration. M3 is the same size with M4 to facilitate layout. The W/L for M1 is 2 so as to increase gain of the amplifier at small size. Besides CTIA and photodiode, the pixel also has a row select (RS) switch to realize row scanning. Transistors M5 (0.7μm / 0.35 μm) and M6 (0.7μm/ 0.35μm) work as RS and there are three different positions for them as shown in Figure 4.4 (b), Figure 4.4 (c) and Figure 4.4 (d). These switches are nMOS transistors and they are very small in size to save space. However, nMOS pass transistors have problems transferring voltages close to V_{DD}. Our previous imager involved in Chapter Three has the structure shown in Figure 4.4 (b): M6 cannot transfer voltage higher than (Vdd-V_{th6}), where V_{th6} denotes the threshold voltage of M6. So the linear range for output voltage ends before 2.3 V according to the simulation result shown in Figure 4.5. The circuit shown in Figure 4.4 (c) has the same problem. To address this problem, the circuit shown in Figure 4.4 (d) was adopted in the second generation image sensor: In this circuit, M6 does not carry the amplifier bias current and the current it carries is no more than the photocurrent, which is so small that M6 continues to work as a pass transistor in the subthreshold region. As a result, the linear range can be extended to 2.7 V according to the simulation result shown in Figure 4.5 at the cost of larger column capacitance. Larger voltage range contributes to higher DR and higher maximum SNR. The two

Table 4.1: Gain and gain-bandwidth (GBW) of amplifiers in pixel circuits and S/H circuits according to simulation results

	Gain	GBW	I
Amplifier in pixel	81dB	106 MHz	200 nA
Amplifier in S/H	82dB	118MHz	356 nA

pMOS transistors M3 and M4 are not in the pixel. They are shared by a whole column so there are only nMOS transistors in a pixel to save space and increase FF.

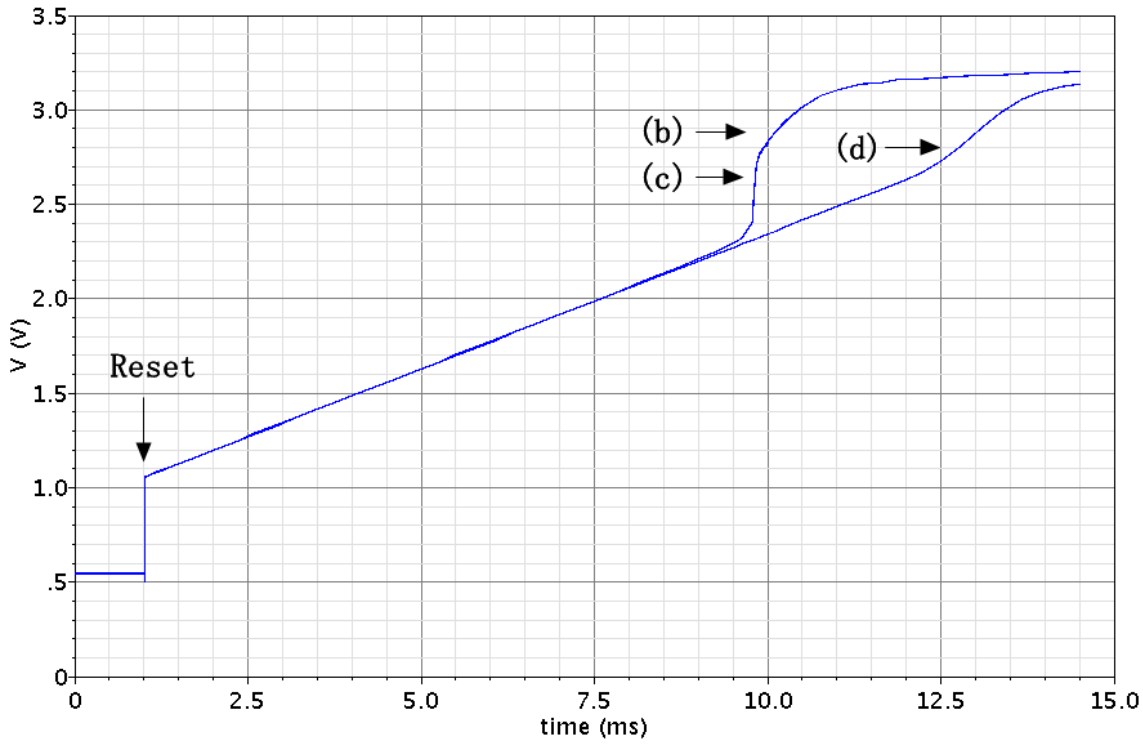

Figure 4.5: Simulation result of the integration course of v_{out} for three different schematics shown in Figure 4.4 (b), (c) and (d). For (b) and (c), v_{out} saturates before 2.3 V while for the circuit in (d), v_{out} saturates at around 2.7 V.

Another method to improve linear voltage range is related with reset voltage which is the gate voltage of M7. The reset voltage of previous imager is V_{DD} and it suffers severe voltage jump caused by charge injection. When the gate voltage of a pass transistor turns from high to low, the

transistor injects negative charges under gate oxide through drain and source terminals. The charges injected to the capacitance at input terminal of amplifier leads to a drop of input voltage and a jump of output voltage. The amount of charges injected mainly depends on reset voltage and transistor size. Lower reset voltage and smaller transistor size correspond to fewer charges. In addition, a smaller C_{fb} leads to higher voltage change according to Figure 4.3. Thus the selection of C_{fb} is a trade-off between high sensitivity and low voltage jump. The reset switch is almost the smallest size possible for this technology. As for reset voltage, according to a simulation result for different reset voltages shown in Figure 4.6, the jump is about 0.5 V when reset voltage is 3.3 V and 0.35 V for 2.5 V reset voltage, and around 0.15 V for 1.7 V reset voltage. The reset voltage cannot decrease limitlessly and it has to be larger than two threshold voltages. As a result, the reset voltage was chose to be 1.7 V.

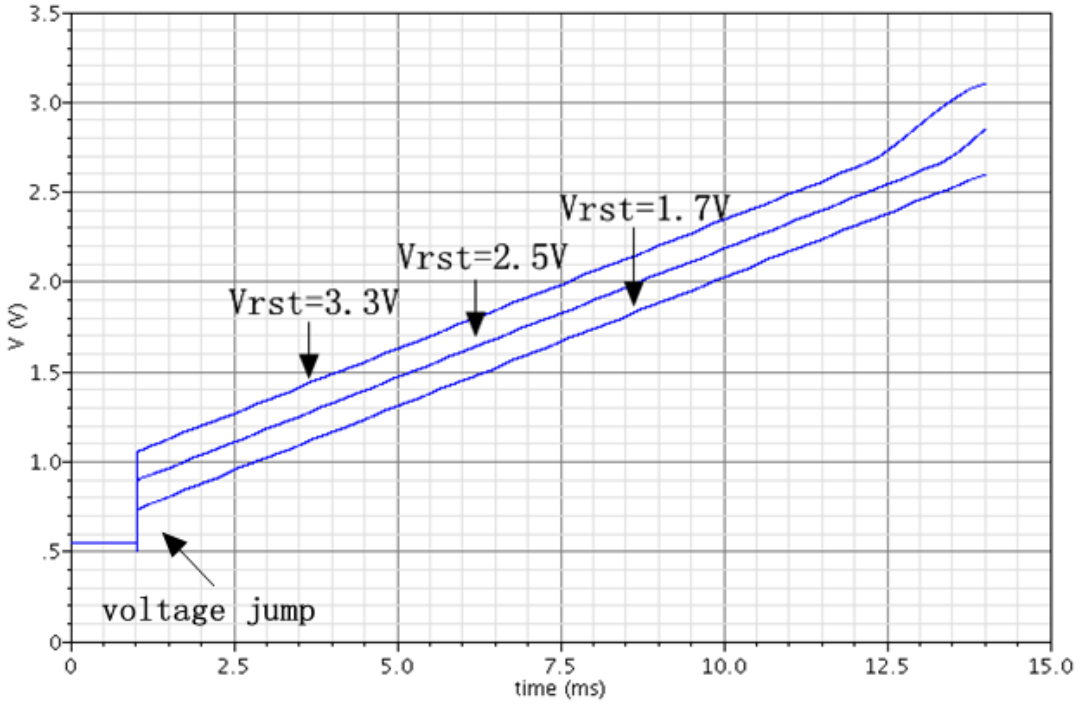

Figure 4.6: Pixel output change vs. time for different reset voltages. The reset is off and integration starts after the first millisecond.

4.1.3 S/H Circuit

There are mainly two kinds of S/H circuits for imagers. One is conventional CDS which samples the difference between signal at end of integration and reset voltage of the same integration cycle. CDS can suppress offset FPN and reset noise because both signal voltage and reset voltage contains the same offset FPN and the same reset noise so they can be cancelled out after subtraction. However, it is not compatible with CTIA-based image sensors or typical 3-T sensors under rolling shutter mode. So another S/H circuit was adopted: It is called double delta sampling (DDS) [59] or delta difference sampling [41] or delta reset sampling [28]. DDS samples the difference between the signal at the end of integration and the next reset voltage while conventional CDS samples reset and signal within one integration cycle. Since signal and reset are not in the same cycle, reset noise actually increases [28]. However, it can still suppress offset FPN effectively, which is important to CTIA-based imager because the C_{fb} is designed to be very small to achieve high sensitivity and so large offset FPN is a more severe problem compared with reset noise.

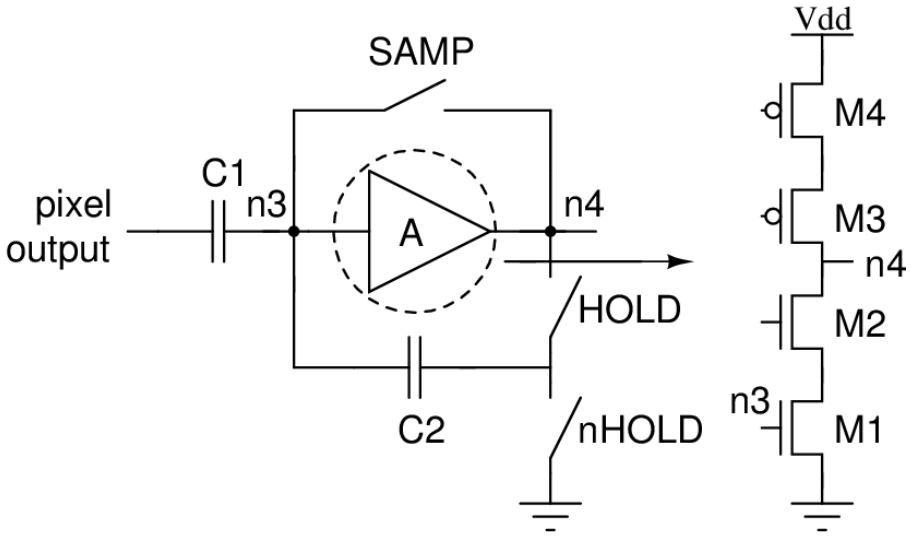

Figure 4.7: Schematic of the S/H circuit.

The schematic of DDS circuit is shown in Figure 4.7. It consists of a cascode amplifier, two capacitors C1 (139 fF) and C2 (139 fF) and three pass transistors working as switches. The cascode amplifier consists of two nMOS transistors M1 (1.4 μm/ 0.7 μm) and M2 (1.4 μm/ 2.1 μm) and two pMOS transistors M3 (2.1 μm/ 1.4 μm) and M4 (2.1 μm/ 1.4 μm).

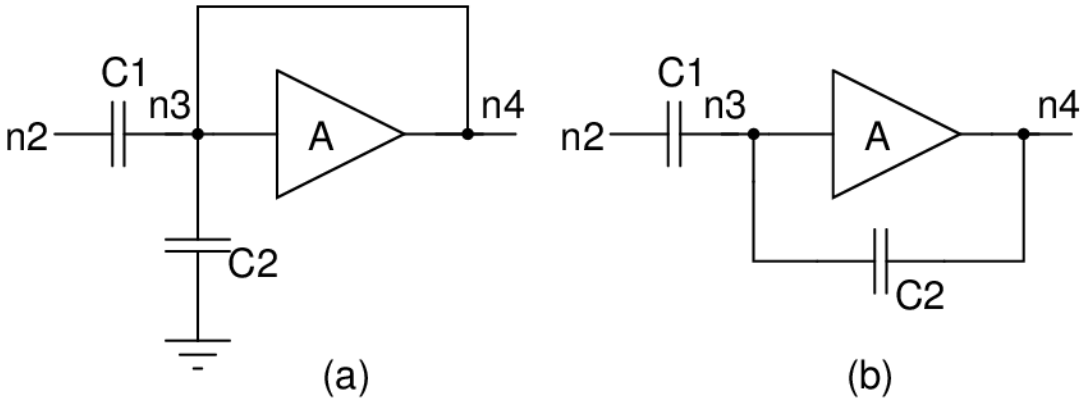

Figure 4.8: Equivalent schematics for the two phases of DDS (a) sample phase, (b) hold phase

The specifications of the cascode amplifier are shown in Table 4.1. It has higher GBW compared with the one in the pixel in order to achieve higher speed at the cost of higher power consumption. The three nMOS pass transistors are very small in size (0.4 μm/ 0.35 μm): One is controlled by sample (SAMP) and the other two are controlled by HOLD and its complementary signal (nHOLD), respectively. The DDS works in two phases: sample and hold. In sample phase, SAMP is high and HOLD is low (thus nHOLD is high), resulting in an equivalent schematic shown in Figure 4.8 (a). DDS enters sample phase at the end of the photocurrent integration to sample the signal. The total charges of C1 and C2 at the end of sample phase is

$$Q_{samp} = (v_{samp} - v_{sig}) \cdot C1 + v_{samp} \cdot C2 \tag{4.5}$$

where v_{sig} represents the signal voltage and v_{samp} denotes the reset voltage of DDS. Then DDS enters hold phase from sample phase: SAMP becomes low and Hold turns high, the output

feedbacks to the input through C2 as shown in Figure 4.8 (b). Once DDS enters hold phase, the pixel circuit is reset by RST signal and the output changes from v_{sig} to reset voltage v_{rst}. Assume the voltage change at terminal n3 is Δv, then the total charges of C1 and C2 in hold phase are given by

$$Q_{hold} = (v_{samp} + \Delta v - v_{rst}) \cdot C1 + (v_{samp} + \Delta v - (v_{samp} - A\Delta v)) \cdot C2 \quad (4.6)$$

When sample phase ends, C1 and C2 are connected to the input of the amplifier so the charges on C1 and C2 have nowhere to flow away, satisfying the charge conservation requirement. If C1 and C2 are equivalent, then we have

$$(v_{samp} - v_{sig}) + v_{samp} = (v_{samp} + \Delta v - v_{rst}) + (v_{samp} + \Delta v - (v_{samp} - A\Delta v)) \quad (4.7)$$

which is simplified as

$$v_{samp} - (A + 2)\Delta v = v_{sig} - v_{rst} \quad (4.8)$$

Given that the gain of cascode amplifier is so high that $A \gg 2$, so it is further simplified to

$$v_{samp} - A\Delta v = v_{sig} - v_{rst} \quad (4.9)$$

The section on the left of the equation is the output of DDS, so we have

$$v_{out} = v_{sig} - v_{rst} \quad (4.10)$$

As a result, DDS outputs the difference between the signal and reset voltage.

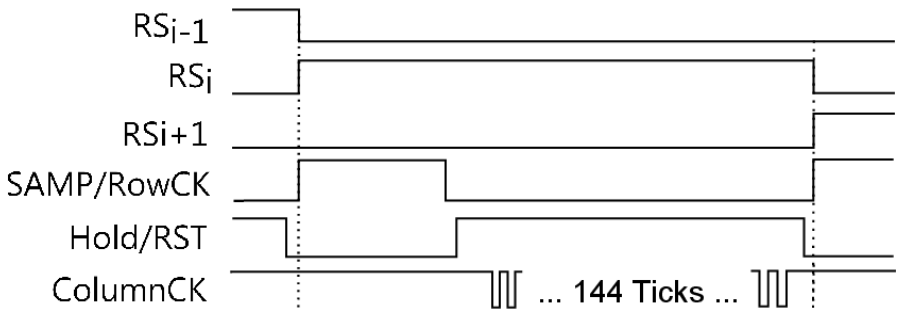

Figure 4.9: Timing diagram showing the sequence of RST, Sample, Hold and Columns in Row (i) and part of Row (i-1) and Row (i+1).

Five control signals are involved to control the pixel and DDS: row clock (rowCK), column clock (ColumnCK), SAMP, HOLD and RST. The time sequence is shown in Figure 4.9. To simplify control signals, rowCK and SAMP share the same signal and RST and HOLD share the same one. SAMP and HOLD have to be non-overlapping signals to satisfy charge conservation requirement. The rowCK selects rows one by one and once a row is selected, DDS samples outputs of all pixels in this row and then holds the difference to be sent out one by one.

4.1.4 Pixel Layout

The layout for two pixels is shown in Figure 4.10. They are symmetric and share the same ground. Each row consists of 72 such pairs, that is, 144-pixel columns. The size of a pixel is 9.5 $\mu m \times 9.5\ \mu m$ and the active area is 23 μm^2, resulting a fill factor of 26%.

A micrograph for the whole CMOS imager chip is shown in Figure 4.11. The square part on the left is the pixel array of 144×144 pixels. The stripes on the right side of the array are 144 DDS circuits and 144 ADCs.

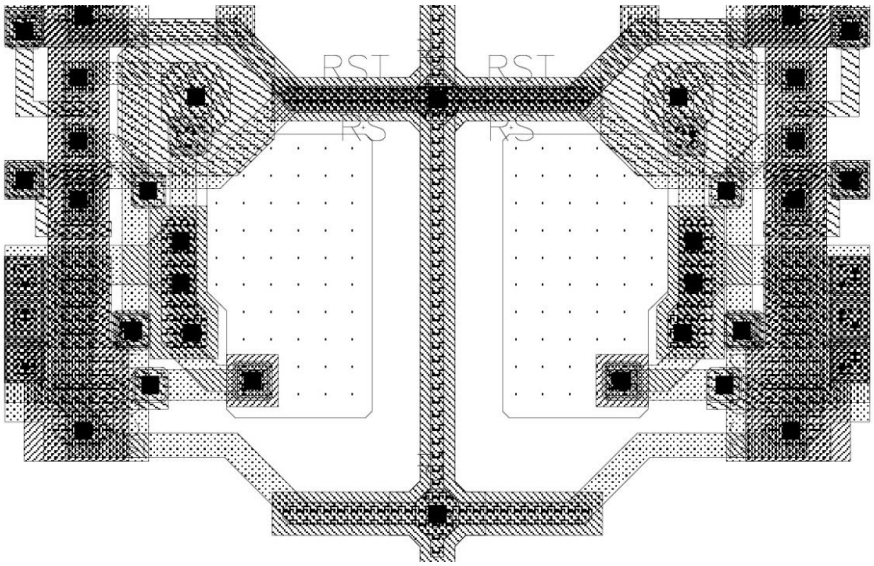

Figure 4.10: Layout for two pixels

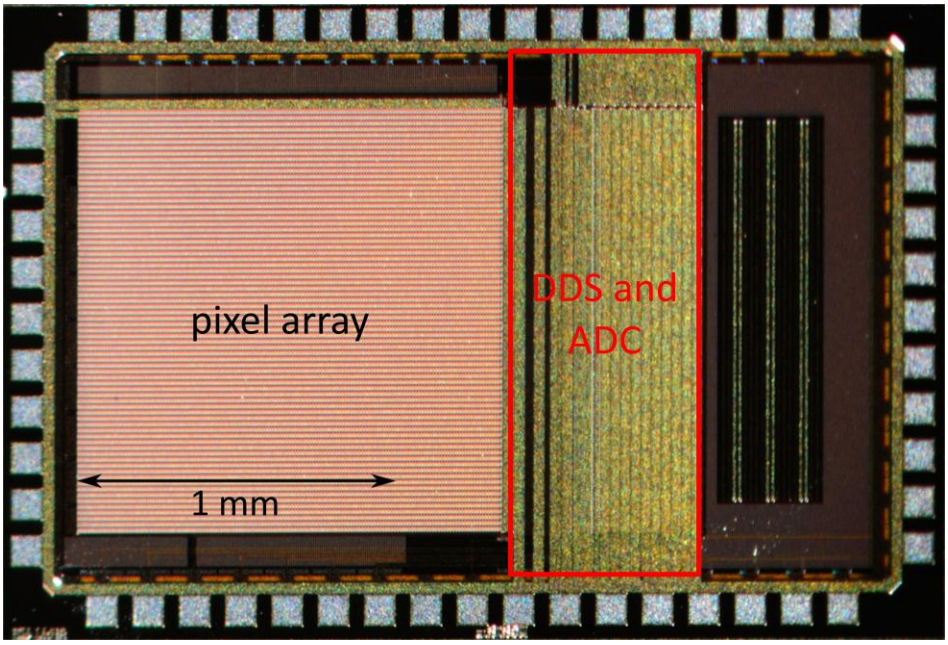

Figure 4.11: Layout for the whole imager chip

4.2 Characterization

To characterize the imager, I made a printed circuit board (PCB) and integrated all components: a 16-bit microcontroller (Microchip, Chandler, AZ) for controlling the imager, two 3.3-V voltage regulators as digital and analog power supplies, and potentiometers to generate biases. Data was collected by a data acquisition (DAQ) device (NI, Austin, TX) with 16-bit ADC. A blue LED with 450 mm wavelength was used for illumination and an integrating sphere was used to generate uniform illumination. The light intensity was measured by an optical power meter. The imager was run at 60 fps. For the characterization of spectrum response, a monochromator was utilized to generate light with different wavelengths.

If not specified, I characterized the central 128×128 pixels of the 144×144 pixel array and ignored pixels at the boundaries to avoid some non-ideal effects such as leakage. According to Figure 4.5 and Figure 4.6, there is a voltage jump at the start of integration so the output of DDS

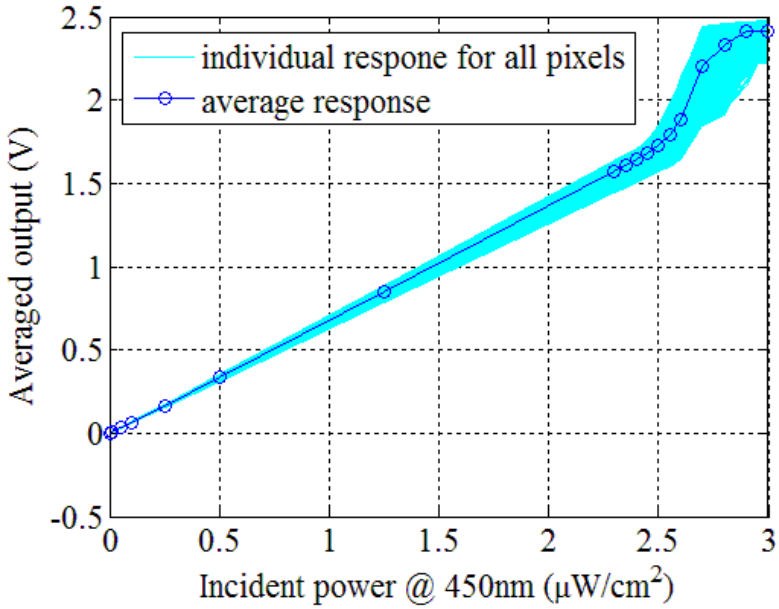

Figure 4.12: Response of all pixels and average response at 450 nm wavelength

is not zero even when integration time is zero. To eliminate this jump, I took images under darkness and subtracted these dark images from test images. As a result, the average outputs of images taken under very low light are close to zero. To characterize response, noise, SNR and FPN performance, I took images of a featureless flat surface under different incident intensities and averaged 100 frames for each light intensity and then plotted all pixel values of the averaged frames on one figure to see how the sensitivity of each pixel differs with each other. The result is shown in Figure 4.12. Some pixels are more sensitive to light while others are less. The variations here show difference on gain FPN as a result of variations of C_{fb}. Averaging all curves into one to offers a mean response. The points on this curve can be expressed as

$$\mu_{overall} = \frac{\sum_{p=1}^{128\times128}\sum_{f=1}^{100}\mu_{p,f}}{100\times128\times128} \tag{4.16}$$

where f represents the number of frames ranging from 1 to 100 and p represents the number of pixels so it is from the first pixel to the 16368-th pixel, $\mu_{p,f}$ denotes the output of the *p-th* pixel on the *f-th* frame. The response is linear when incident power is below 2.45 μW/cm^2. For stronger illumination, the output rises up much rapidly and finally the output saturates. The maximum output in linear range is 1.68 V.

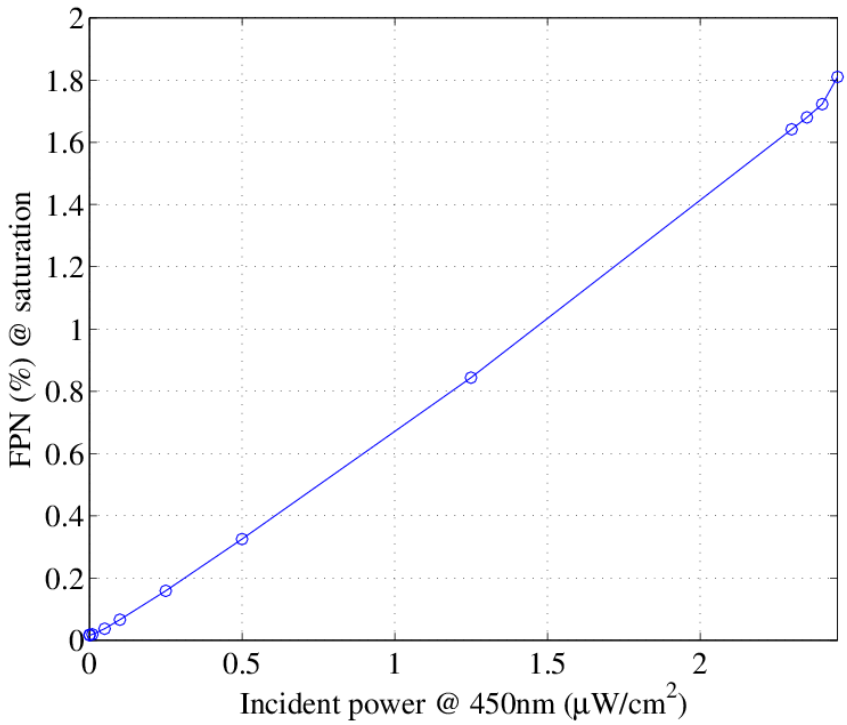

Figure 4.13: FPN for different incident powers

As mentioned before, offset FPN has been eliminated by DDS. The variation of response shown in Figure 4.12 is a result of gain FPN. It was characterized by creating one averaged image over 100 frames and then calculating the spatial standard deviation over all pixels in this image. Then it was normalized by the saturation voltage so we can see how the spatial variation compares with the saturation voltage. The calculation was done at each light intensity. As can be seen in Figure 4.13, the FPN increases linearly with incident light power in the linear response

range and it reaches 1.8 % at the incident power of 2.45 μW/cm^{-2}, which is the end of linear response range and we defined it as photo response non-uniformity (PRNU). Similarly, when incident power is zero, we have the dark signal non-uniformity (DSNU), which is 0.02%.

We also characterized the spectral response shown in Figure 4.14. The wavelength ranges from 400 nm to 1100 nm and the response peaks at 775 nm. The response decreases rapidly near 1100 nm because this wavelength corresponds to the energy bandgap and photons with higher wavelength cannot generate photocurrents.

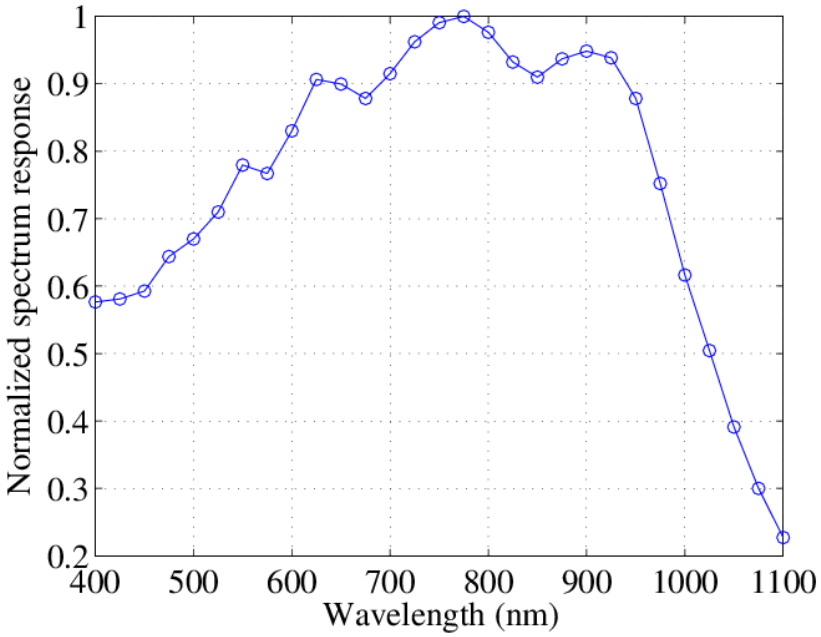

Figure 4.14: Normalized Spectrum response: Wavelength is from 400 nm to 1100 nm and the response peaks at 775 nm.

Figure 4.12 and Figure 4.14 show sensitivity characteristic of the imager. In literature, there are a couple of definitions of sensitivity [50]. One definition is in terms of incident power, that is, the voltage output of one pixel exposed to the incident power of 1 μW/cm^2 for 1 second.

According to Figure 4.12, the output is 1.68 V when incident light intensity is 2.45 μW cm^{-2} at 60 fps, so sensitivity is calculated accordingly

$$\text{Sensitivity} = \frac{1.68}{2.45} * 60 = 41.1\ \text{V} \cdot \mu\text{W}^{-1} \cdot \text{cm}^2 \cdot \text{s}^{-1} \tag{4.17}$$

This is the sensitivity for the wavelength of 450 nm. According to the normalized spectrum response shown in Figure 4.14, the sensitivity corresponding to the wavelength of 550 nm is calculate as 71.3 V ·μW^{-1} cm^2 s^{-1}. Another commonly used definition adopted in literature is in terms of illuminance, that is, the voltage output of a pixel exposed to the illumination of 1 lux for 1 second. Under this definition, the sensitivity is 10.44 V ·lux^{-1} s^{-1}. However, these definitions do not take the size of pixels into account. Consider two pixels, the design of which has everything in common except for the photodiode size: The larger pixels with a larger photodiode is expected to have high sensitivity because it has more area exposed to light and thus samples more photons compared with smaller ones in spite of the same design in other aspects. So we normalized the sensitivity defined above with pixel sizes to facilitate the comparison of sensitivity. Under this definition, the sensitivity is 790 mV ·μW^{-1} cm^2 ·μm^{-2} s^{-1} for 550 nm wavelength and 460 mV ·μW^{-1} cm^2 ·μm^{-2} s^{-1} for 460 nm wavelength.

Figure 4.15: Flow chart showing QE determines the conversion process from light to electrons and conversion gain determines the conversion from electrons to voltage.

Sensitivity mainly depends on two factors: quantum efficiency (QE) and conversion gain. As shown in Figure 4.15, QE is the ratio of the number of electron-hole-pairs (EHP) to the number

of incident photons. It is always smaller than 1 because of the nature of light. Conversion gain is defined as the output change caused by one electron. This process occurs on capacitors. The change of charges on capacitance leads to voltage change. In our case, this process happens on C_{fb}. So the conversion is calculated as follows

$$\text{Conversion gain} = \frac{Q_e}{C_{fb}} = \frac{1.6\times10^{-19}}{2.1\times10^{-15}} = 76\ \mu\text{V/e}^- \tag{4.18}$$

where Q_e denotes the charge of one electron. Given than output voltage is 1.68 V at incident light intensity of 2.45 $\mu W/cm^2$, we can calculate QE according to the expression below

$$\frac{\text{I}_{\text{light}}\cdot(\text{pixel area})\cdot(\text{exposure time})}{\frac{\text{hc}}{\lambda}} \cdot \text{QE} \cdot (\text{Coversion gain}) = \text{V} \tag{4.19}$$

where I_{light} is light intensity 2.45 $\mu W/cm^2$, h refers to Planck's constant, c is the speed of light in vacuum, λ is the wavelength of 450 nm, exposure time is 16.7 ms for the speed of 60 fps and V refers to 1.68V. As a result, QE is calculated as 26.5%. In addition, full well capacity is an important parameter characterizing the maximum charges one pixel can accommodate. It is given by

$$\text{full well capacity} = \frac{satuarton\ volatge}{conversion\ gain} = \frac{2.4}{76\times10^{-4}} = 3.2\times10^4 \tag{4.20}$$

Here 2.4 V is the saturation voltage according to Figure 4.12, and the full well capacity is $3.2 \times 10^4\ e^-$.

The temporal noise is calculated using the frames acquired before, that is, for each incident light intensity level I took 100 frames and then calculated the standard deviation over the 100 -frames for each pixel. As a result, we had 128*128 standard deviations. Then we could get the overall temporal noise by adding the standard deviations of the 128×128 pixels in quadrature, which is given by:

$$\text{noise} = \sqrt{\frac{\sum_{p=1}^{128\times128} \sigma_p{}^2}{128\times128}} \tag{4.21}$$

where σ_p is the standard deviation of pixel p over 100 frames. The result is plotted in Figure 4.16, when there is no incident light, the total output referred noise is about 2 mV, which is basically read noise caused by thermal movement of electrons in electronic devices in the system. With the increase of incident power, the noise increases with a decreasing slope because shot noise starts to manifest. When incident power becomes around 2.4 $\mu W/cm^2$, there is a surge of noise because linear range ends and the response slope of becomes much bigger so the standard deviation also increases. After 2.7 $\mu W/cm^2$ the noise drops down because pixels start to be saturated and the output then stays constant regardless of the increase of incident power.

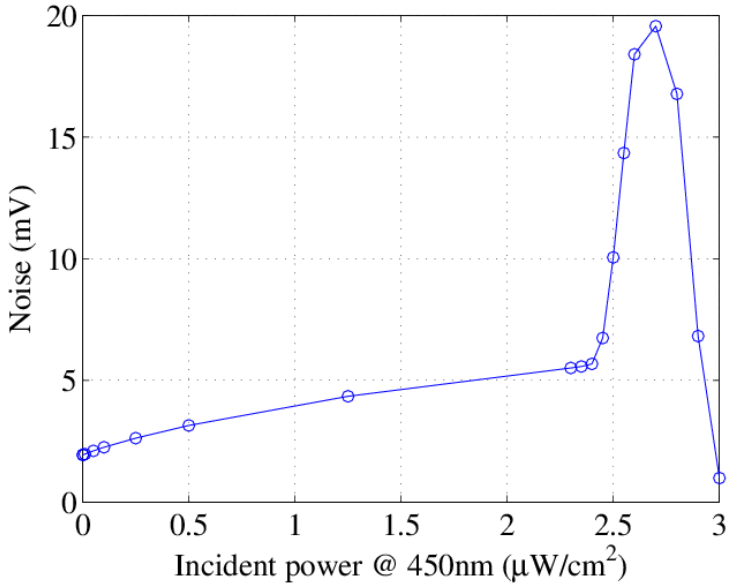

Figure 4.16: The noise performance of the imager at different incident power under the wavelength of 450nm.

With the information of averaged output and noise we can get the SNR plotted in Figure 4.17. In the linear response range, SNR increases with incident power and reaches 49 dB when

incident power is 2.45 μW/cm^2. The minimum detectable signal equals to noise, that is, when SNR = 0 dB. According to Figure 4.17, the minimum detectable signal is 2.3 nW/cm^2 and we can calculate the minimum number of photons for one pixel at the speed of 60 fps as

$$\frac{I_{light\ (min)} \cdot (\text{pixel area}) \cdot (\text{exposure time})}{hc/\lambda} = 78 \qquad (4.22)$$

Given that maximum incident power is 2.45 μW/cm^2 within linear range, the dynamic range (DR) is calculated as 61 dB. The summary of specifications of the imager is shown in Table 4.2.

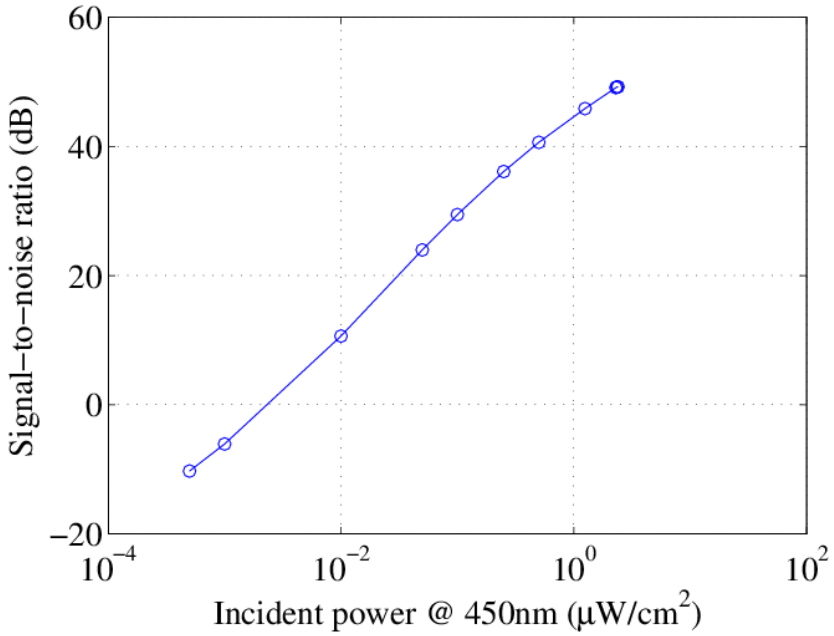

Figure 4.17: SNR vs. incident power: in linear range, SNR increases with incident power and reaches 49 dB at incident power of 2.4 μW/cm^2

According to Table 4.3, the second generation image sensor has several improvements compared with the first generation: The second generation is based on a different technology and has smaller pixel size. The linear range is greatly increased as a result of the two improvements in pixel circuit design. The SNR and DR are increased. The power consumption is reduced due

to the optimization of amplifiers and the sensitivity is increased. The minimum detectable intensity depends on wavelength, pixel size and framerate so it is hard to make a comparison directly. So we normalized it with the three factors and the parameter after normalization is the minimum detectable number of photons. The second generation can detectable obviously less photons, implying a stronger ability of low light imaging.

Table 4.2: Parameters for the image sensor described in this paper

Parameter		Value
Technology		0.35 μm
Pixel type		CTIA
Pixel count		144×144
Pixel pitch		9.5 μm×9.5 μm
Fill factor		26%
Frame rate		60 fps
DR		61 dB (linear range)
Sensitivity (550 nm)		10.44 V·lux^{-1}·s^{-1} 790 mV·μW^{-1}·cm^{2}·μm^{-2}·s^{-1}
SNR		49 dB (linear range)
FPN	DSNU	0.02% (of saturation)
	PRNU	1.8% (of saturation)
Minimum detectable intensity		2.3 nW·cm^{-2}
Minimum detectable number of photons (after normalizing minimum detectable intensity by size, wavelength and framerate)		78
Conversion gain		76 μV/e^{-}
Power supply		3.3 V
Saturation voltage		2.4 V
Linear range		1.68 V
Power consumption		270 μW (analog) and 284 μW (digital)
Full well capacity		32,000 e
QE		26.5%

Table 4.3: A comparison between first generation image sensor and second generation image sensor

Parameter	First generation	Second generation
Technology	0.5 μm	0.35 μm
Pixel size	20 μm	9.5 μm
Linear voltage range	0.3 V	1.7 V
Maximum SNR	44 dB	49 dB
Dynamic Range	50 dB	61 dB
Power consumption	2.4 mW @ 70 fps	0.55 mW @ 60 fps
Normalized sensitivity	0.7	1
Minimum detectable intensity	4 nW cm^{-2} @ 70 fps	2.3 nW cm^{-2} @ 60 fps
Minimum detectable number of photons (after normalizing minimum detectable intensity by size, wavelength and framerate)	560	78

Table 4.4 shows a comparison table between our imager and some other recently published imagers on some typical specifications to provide a general idea on the range of this parameters [51]-[55]. The imagers involved are designed for different aims such as high DR, high resolution and so on. We can see the advantage of high sensitivity of our imager is obvious compared with other imagers, which is critical for low light biomedical imaging.

Table 4.5 shows a comparison between our imager described in current chapter, the imager described in Chapter Three [41] and some other imagers designed specifically for high sensitivity and low-light imaging [56]-[58]. The minimum detectable intensity parameter is frame rate and pixel size dependent, so high-speed imagers have a relatively poor performance. The photon count parameter normalizes the minimum detectable intensity in terms of pixel area, frame rate and wavelength and is shown in the form of the minimum number of photons

Table 4.4: A comparison between our imager with some recently published imagers on some key specifications

	this work	[51]	[52]	[53]	[54]	[55]
Year published	2014	2008	2011	2011	2012	2012
Technology	0.35 μm	0.35 μm	0.5 μm	0.13 μm	0.35 μm	0.18 μm
Pixel type	CTIA	3T	4T	3T	3T	4T
Pixel count	144×144	160×240	54×50	1696×1212	100×100	1032×1024
Pixel size (μm)	9.5×9.5	5.6×5.6	21×21	2.25×2.25	30×30	7.5×7.5
Fill factor	26%	32%	32%	N/A	44%	52%
Frame rate (fps)	60	-	7.4	240	500	4
DR (dB)	61	68	58.7	59	-	82
Sensitivity ($V\ lux^{-1}\ s^{-1}$)	10.44	0.44	0.38	0.69	-	10
Conversion gain ($\mu V/e^-$)	76	48	1.76	80	4.9	67
power supply (V)	3.3	3.3/1.8	1.2	2.8 /1.5	-	-
full well capacity (e^-)	3.2×10^4	2.0×10^4	3.96×10^5	1.1×10^4	2.56×10^5	1.5×10^4

Table 4.5: A comparison between our imager with some high-sensitivity imagers designed for low-light imaging

	this work	[56]	[57]	[41]	[58]
Year published	2014	2006	2007	2011	2012
Technology	0.35 μm	0.18 μm	0.25 μm	0.5 μm	0.18 μm
Pixel count	144×144	8×16	514×530	132×124	256×256
Pixel size (μm)	9.5×9.5	240×210	20×20	20×20	15×15
Fill factor	26%	45 %	40 %	42 %	37 %
DR (dB)	61	61	60	48	56.5
Sensitivity ($V\ lux^{-1}\ s^{-1}$) (approximately 550 nm)	10.4	160	19.9	-	35.1
Normalized sensitivity ($mV\cdot\mu W^{-1}\ cm^2\cdot\mu m^{-2}\ s^1$) (approximately 550 nm)	790	22	341	-	1070
Frame rate (fps)	60	0.03	3500	70	1500
Power consumption (mW)	0.55	26 (ADC)	1000 (ADC)	2.4	390 (ADC)
Wavelength (nm)	450	562	-	450	560
Minimum detectable intensity	2.3 nW/cm^2	0.15 pW/cm^2	-	4 nW/cm^2	0.15 $\mu W/cm^2$
photon count	78	640	-	560	636

detectable. Compared to the first generation CTIA imager that the current design is based on, we have a considerable improvement in terms of DR, power consumption, minimum detectable light intensity and minimum detectable photon count.

4.3 The second generation system and DBS experiment

4.3.1 System overview

The second generation imaging system is shown in Figure 4.18. It consists of the imager chip and its package, a microcontroller, potentiometers to generate biases and a miniaturized optical system. As shown in Figure 4.18, the new generation miniaturized optical system is supported by two-cylinder structure. The cylinder on the outside is fixed one imager package while the other one inside contains a lens inside and it can move up and down to adjust the distance between lens and imager for focusing. It also has four LEDs (two symmetric blue LEDs and two symmetric green LEDs) on top for illumination so it is expected to achieve better illumination uniformity compared with the previous version. The light intensity of the LED is controlled by pulse width modulation (PWM) function of the microcontroller, so we did not need specific LED drives, thus saving size and cost. Compared with the previous optical system measured 18 mm in diameter and 12 mm in height, the new generation optical system is 10 mm in diameter and 11 mm in height. Seven potentiometers are used to provide biases. The voltage regulator on the left is an adjustable one generating reset voltage for pixel circuits so as to increase voltage range and the other two are analog and digital power supply, respectively.

The imaging system is designed and fabricated for testing purpose: First, it is critical to see if the imager works as expected under the control of microcontroller. Second, we need to figure out

the best biases for the imager by adjusting potentiometers. In addition, A proper reset voltage can be determined. Finally, the system is used to test the second generation optical system.

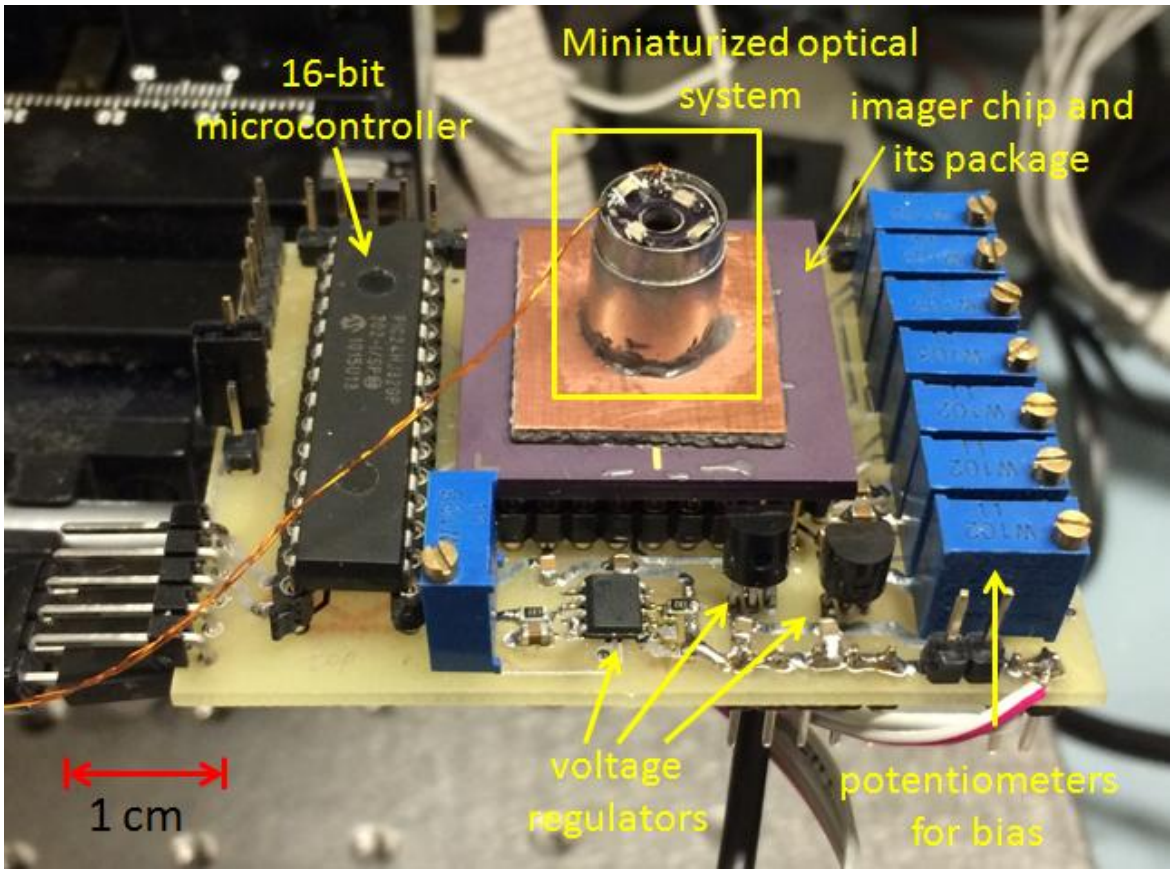

Figure 4.18: The imaging system consists of the imager chip and its package, a microcontroller, potentiometers to generate biases and a miniaturized optical system. The smaller cylinder of the miniaturized optical system can be moved to adjust the distance between lens and imager for focusing. It also has four LEDs (two symmetric blue LEDs and two symmetric green LEDs) on top for illumination. Seven potentiometers are used to provide biases. The voltage regulator on the left is an adjustable one generating reset voltage for pixel circuits so as to increase voltage range and the other two are analog and digital power supply, respectively.

Another important issue regarding the miniaturized system for biomedical application is to get rid of cables connecting the imaging system and benchtop instruments so as to image on freely-moving animals. Battery can be utilized to remove the connection between imaging system and

power supply, which is easy to be realized because the system has voltage regulators in it. The other connection is between imaging system and benchtop DAQ device and computers. Using a microSD card as data storage is a good alternative to remove this connection. We designed a test board as shown in Figure 4.19. It consists of a 16-bit micro-controller working both as a ADC (the ADC in the imager does not work properly) and the controller of the microSD card, two 3.3-V voltage regulators as digital and analog power supplies, one adjustable voltage regular providing reference voltage for ADC and a microSD card socket to hold microSD card. The power comes from the imager board and regulated by voltage regulators. The output of imager is sampled and digitized by an 8-bit ADC module in micro-controller and stored in microSD card through Serial Peripheral Interface (SPI) inference. The number of bits here is limited by data transfer speed.

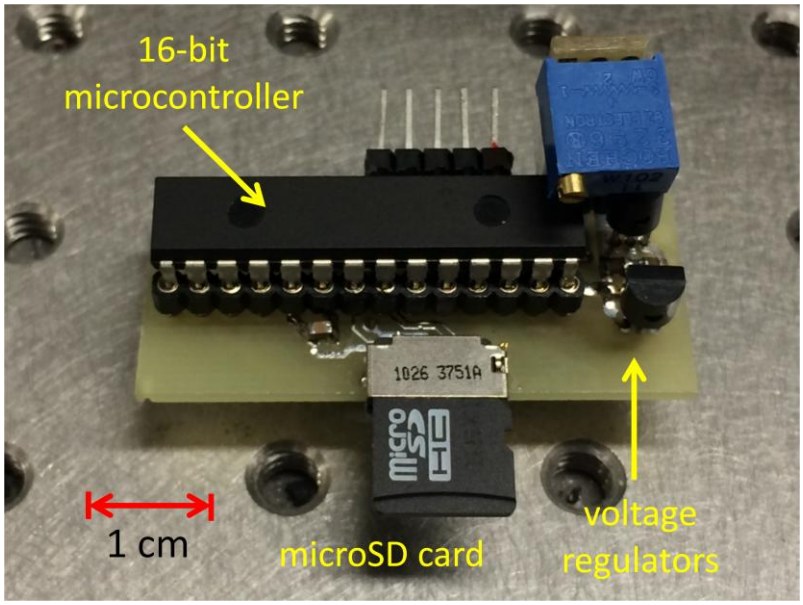

Figure 4.19: Test board consists of a 16-bit micro-controller working both as ADC and microSD card controller, two 3.3-Vvoltage regulators as digital and analog power supplies, one adjustable voltage regular providing reference voltage for ADC and a microSD card socket to hold microSD card.

4.3.2 System characterization

The system consists of the imager board shown in Figure 4.18 and microSD card board shown in Figure 4.19 and some wires connecting them. All the characterization results are based on data stored in microSD card.

4.3.2.1 Illumination uniformity

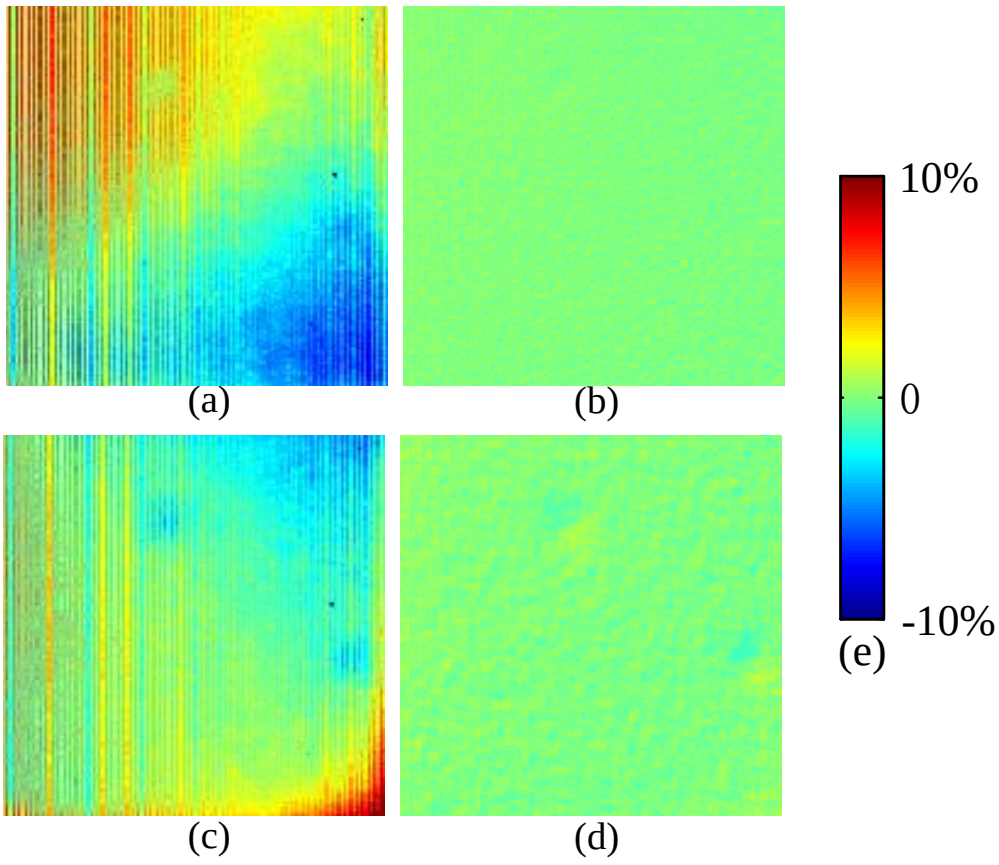

Figure 4.20: (a) Raw image of a featureless flat surface taken under blue light illumination showing illumination non-uniformity measured as relative deviation from the mean of the entire image, (b) two-point calibrated image of (a),(c) raw image of a featureless flat surface taken under blue light illumination showing illumination non-uniformity measured as relative deviation from the mean of the entire image, (d) two-point calibrated image of (c), and (e) color bar using different color to indicate deviation levels.

The illumination of this system is expected to be more uniform that the previous one because it has two symmetric blue LEDs and two symmetric green LEDs for illumination while the previous version has only one LED for each wavelength. Illumination of this system is characterized the same way as Chapter Three and the results are illustrated in the form of colormap. Figure 3.2 (a) shows the raw result under blue light and (b) for green light. The column pattern mainly comes from the symmetric layout of pixels as shown in Figure 4.10, which leads to difference in response of odd and even columns. Figure 3.2 (c) and (d) show results after two-point calibration under blue and green light, respectively. Figure 3.2 (e) shows a color bar using different colors to indicate different levels of non-uniformity. Compared with the illumination uniformity of the previous system which ranges from -50% to 50%, this system has much improved uniformity which falls into the range of -10% to 10% and the overall standard deviation to the mean is 3.3% for Figure 3.2 (a) and 2.4% for Figure 3.2 (b), which are only 15% of the previous system. After calibration, the result becomes 0.23% for blue light and 0.32% for green light, about half of the previous version.0.23%

4.3.2.2 Resolution

A 1951 USAF resolution chart was used again to characterize the resolution of the system. As shown in Figure 4.21 (a), the ideal light intensity along the vertical red line which was added to cross 5 elements from No.2 to No.6 in Group 5 is shown Figure 4.21 (b). Then we took images of the 1 mm × 1 mm region indicated by a red square shown in Figure 4.21 (c) and plotted light intensity along the red line again. The result is shown Figure 4.21 (d): From element 2 to element 5, we can clearly distinguish two peaks from three valleys while for element 6, it is not distinctive. This result indicates a resolution of 51 line pairs/mm or 9.8 μm, which is limited by

the pixel size of 9.5μm. In other words, the optical module of the system does not degrade image quality in terms of resolution.

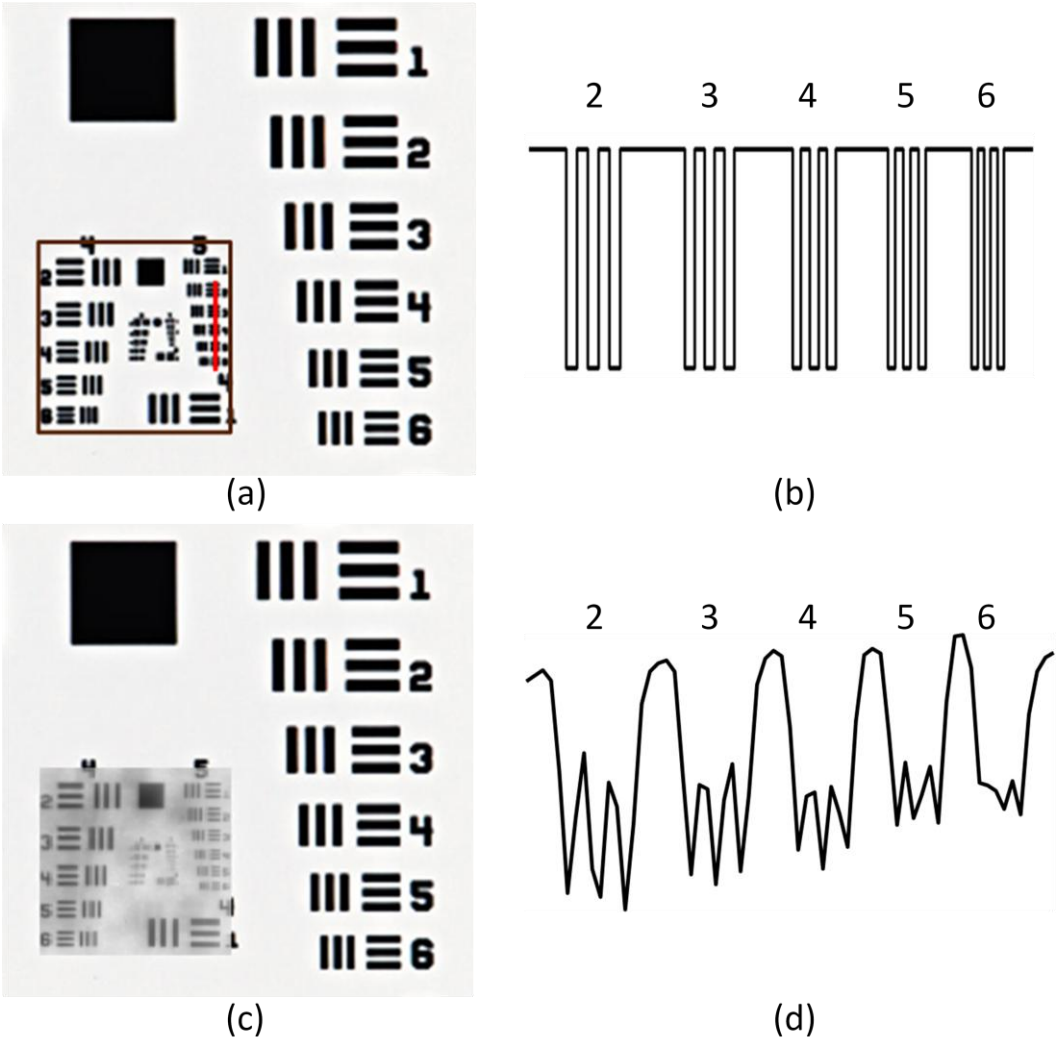

Figure 4.21: (a) 1951 USAF resolution chart, 1 mm × 1 mm red square indicates the region to be imaged, (b) the ideal intensity along the red vertical line, (c) 1951 USAF resolution chart with the actual image taken by the system in the red square outlined and (d) the actual intensity showing resolution limitation.

4.3.3 DBS experiment procedure and result

After fabricating and characterizing the imaging system, we need to use this system to image the reflectance changes related to hemodynamic changes in response to DBS to see if the system has the required sensitivity. The theory is described in Chapter Three and wavelengths (470 nm and 570 nm) and DBS parameters and the electrode position are the same with previous experiment. Again, the primary motor cortex was imaged. Ten images were taken every second and wavelength alternated every 1.5 seconds, so each wavelength cycle is 1.5 seconds. Figure 4.22 shows the image for the tissue and the 100 μm ×100 μm red square was chosen as ROI for subsequent analysis. Similar with the procedure described in Chapter Three, we performed spatial average over ROI for each frame and calculated the temporal average and standard deviation over spatial averages within each wavelength illumination cycle. As a result, we had 1 mean and 1 standard deviation for each cycle. The mean shows overall reflectance of one cycle while the standard deviation contains temporal noise and intensity changes.

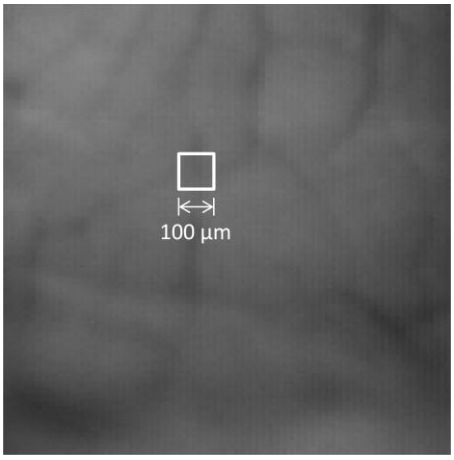

Figure 4.22: A typical image of primary motor cortex taken by the system and the red square shows our ROI to be analyzed

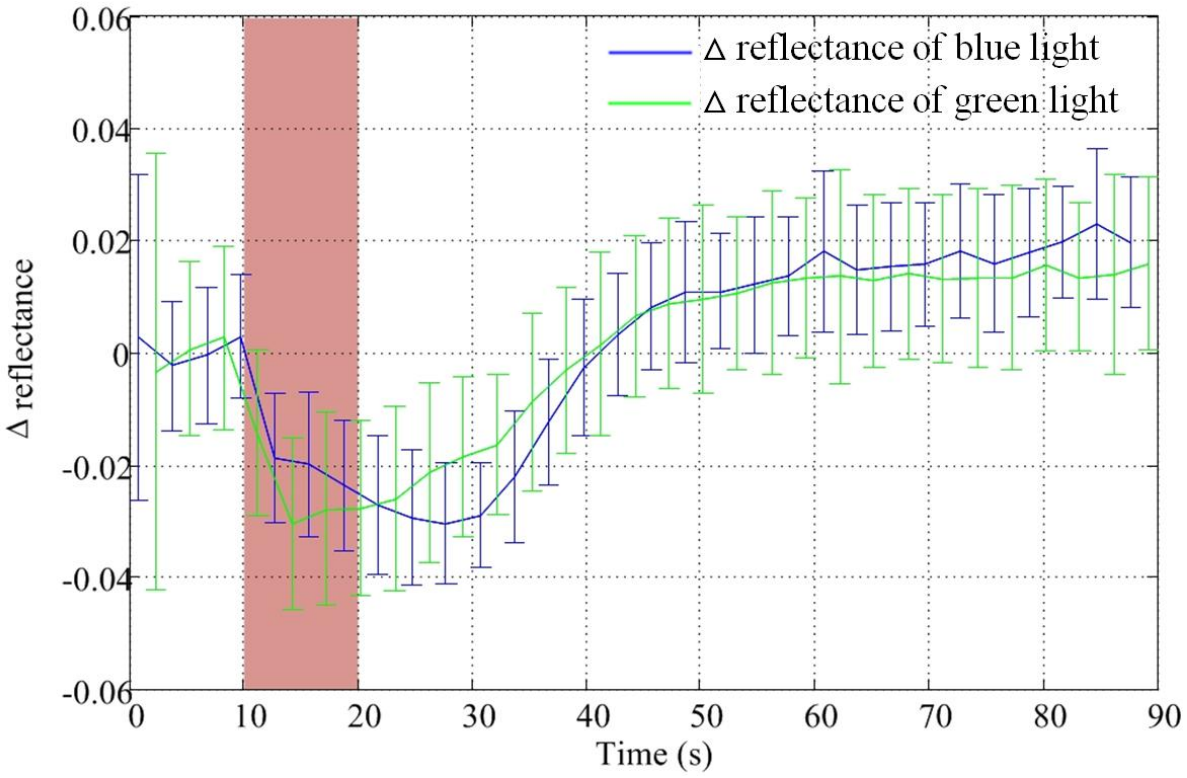

Figure 4.23: The Δ reflectance is plotted in the form of normalized mean ± std of the data with DBS from 10s to 20s indicated by red band. The data of the first 10s were used to normalize mean and standard deviation to show relative change of reflectance. Reflectance for both wavelength decreases once DBS starts and the maximum reduction is about 3% for both wavelengths. Then reflectance increases and stays at a higher level compared with the condition before DBS. Red bar from 10s to 20s indicates DBS.

The data of the first ten seconds (before stimulation starts) was used to normalize all the mean and standard deviations and the change in reflectance, denoted by Δ reflectance, in the form of mean ± standard deviation is shown in Figure 4.23. The reflectance for both blue and green light decreases once the DBS starts, at first reflectance for green light decreases more than blue light while soon after DBS ends, reflectance for blue light becomes lower than green light. The lowest reflectance for green light appears about 4 seconds after DBS starts and for blue light, the lowest reflectance appears about 7 seconds after DBS ends. Then reflectance for both light rises up to an

even higher level than the baseline. It requires a longer observation time to see if the reflectance will finally resume to the baseline.

As with the data shown in Chapter Three, the system is capable of detecting reflectance changes in response to DBS. However, there are differences: the changes are about three-fold larger and there is a crossing over point for the reflectance values in the two channels. While some of this is attributable to animal-to-animal variance, it is worth noting that these are raw reflectance values and no attempt was made to extract the changes in blood volume or the oxygenation. Thoough the simplified Beer-Lambert law based analysis presented in Chapter Three is useful to get an intuitive idea that these reflectance changes are indeed related to vascular changes, detailed non-linear modeling is required to accurately map the information. However, the focus of the research presented in this thesis is to create a system is capable of imaging reflectance changes related to changes in tissue hemodynamics in response to DBS through spectroscopic imaging. Interpreting the reflectance data to discuss the hemodynamic parameters or trying to use those to explain possible mechanisms of DBS is beyond the scope of this work.

Chapter Five: Conclusion and Future Directions

5.1 Conclusion of research presented in the thesis

The research described in this thesis involved four steps towards the eventual goal of creating high-performance and stand-alone CMOS imaging system for imaging reflectance changes related to hemodynamic changes in tissue, specifically the brain tissue oxygenation and blood volume, in response to DBS in awake and freely-moving rats.

The first step was to design a miniaturized optical system and integrate it in an existing imaging system. Then the system was characterized and utilized in an experiment to see if it is able to record changes in reflectance that are related to changes in tissue hemodynamics in response to DBS. The experiment results indicated that both the concentration of oxygen in blood and the blood volume in primary motor cortex increase in response to DBS.

The second step was the design of second generation CMOS imager to achieve higher performance. According to characterization results shown in the thesis, it has higher SNR, DR, lower minimum detectable intensity and power consumption and better resolution performance compared with the previous version of imager involved in the first step.

The third step was the design of second generation imaging system based on the second generation CMOS imager. This system includes a second generation miniaturized imaging system which provides more uniform illumination in smaller size. In addition, the system includes a microSD card board for data storage so the cable connecting the system with a computer is not needed. The voltage regulators in the system enable using battery as power supply so the system can realize stand-alone operation without connecting to benchtop instruments.

The fourth step was to test the second generation imaging system. It was used to image primary motor cortex of a rat to detect changes in tissue reflectance in response to DBS in thalamus. The data was stored in microSD card and later analyzed in a computer. Even with the stand-alone system, it was shown that the system could detect reflectance changes, that are related to tissue oxygenation and blood volume, in response to DBS.

5.2 Future directions

The thesis describes some fundamental work towards stand-alone imaging system capable of imaging in awake and freely-moving animals. The next step is to create the miniaturized imaging system by replacing the components in the system with small-footprint version and minimizing the printed circuit board (PCB). Specifically, it includes removing the package of the imager chip and mount the chip directly on the surface of the PCB, using surface-mount microcontrollers instead of through-hole ones and using digital-to-analog converter (DAC) for biases of the chip instead of big-size potentiometers. The estimated PCB size is around 2 cm^2 for the imager board and around 1 cm^2 for the storage board. Then the imager board and the optimized optical system can be integrated to be mounted on a rat's head and the storage board and a battery can be fixed on the body of the rat. Since the battery and storage board are small and light so it is unlikely to have much effects on the rat's movement.

Besides, the second-generation imager can also be modified. The modification is expected to integrated biases inside the chip using resister ladder so bias generators such as DAC or potentiometers can be removed to save space.

On the experimental side of things, more work can be done on building realistic and accurate mathematic models to extract oxygenation and blood volume changes from the dual-wavelength

reflectance data. Then the imaging system can be utilized alongside monitoring arterial blood gas (ABG) approach to test the validity of the mathematic models and the sensitivity and accuracy of this approach.

References

[1] Perlmutter, Joel S., and Jonathan W. Mink. "Deep brain stimulation." *Annu. Rev. Neurosci*., vol. 29 (2006): 229-257.

[2] Kringelbach, Morten L., Ned Jenkinson, Sarah LF Owen, and Tipu Z. Aziz. "Translational principles of deep brain stimulation." *Nature Reviews Neuroscience,* vol. 8, no. 8 (2007): 623-635.

[3] Montgomery, Erwin B., Matthew B. Stern, Kenneth A. Follett, and Frances M. Weaver. "Randomized trial of deep brain stimulation for Parkinson disease: Thirty-six-month outcomes; Turning tables: Should GPi become the preferred DBS target for parkinson disease?." *Neurology*, vol. 80, no. 2 (2013): 225-225.

[4] Winegar, Bruce D., and M. Bruce MacIver. "Isoflurane depresses hippocampal CA1 glutamate nerve terminals without inhibiting fiber volleys." *BMC neuroscience*, vol. 7, no. 1 (2006): 5.

[5] Berg‐Johnsen, J., and I. A. Langmoen. "The effect of isoflurane on excitatory synaptic transmission in the rat hippocampus." *Acta anaesthesiologica scandinavica,* vol. 36, no. 4 (1992): 350-355.

[6] Shahrokhi, Farzaneh, Karim Abdelhalim, Demitre Serletis, Peter L. Carlen, and Roman Genov. "The 128-channel fully differential digital integrated neural recording and stimulation interface." Biomedical Circuits and Systems, IEEE Transactions on 4, no. 3 (2010): 149-161.

[7] Kussener, E., T. Barroca, B. Lincoln, P. Salin, C. Forni, O. Mainard, H. Barthelemy, and D. Goguenheim. "Integrated continuous microstimulation system for deep brain stimulation in rodent models of neurological disorders." *8th IEEE International NEWCAS Conference (NEWCAS)* (2010): 1-4. [8] Shahrokhi, Farzaneh, Karim Abdelhalim, Demitre Serletis, Peter L. Carlen, and Roman Genov. "The 128-channel fully differential digital integrated neural recording and stimulation interface." *IEEE Transactions on Biomedical Circuits and Systems,* vol. 4, no. 3 (2010): 149-161.

[8] Perlmutter, J. S., J. W. Mink, A. J. Bastian, K. Zackowski, T. Hershey, E. Miyawaki, W. Koller, and T. O. Videen. "Blood flow responses to deep brain stimulation of thalamus." *Neurology,* vol. 58, no. 9 (2002): 1388-1394.

[9] Perlmutter, Joel S., and Jonathan W. Mink. "Deep brain stimulation." *Annu. Rev. Neurosci.,* vol. 29 (2006): 229-257.

[10] Kringelbach, Morten L., Ned Jenkinson, Sarah LF Owen, and Tipu Z. Aziz. "Translational principles of deep brain stimulation." *Nature Reviews Neuroscience,* vol. 8, no. 8 (2007): 623-635.

[11] Zhang, Xiao, Muhammad S. Noor, Clinton B. McCracken, Zelma HT Kiss, Orly Yadid-Pecht, and Kartikeya Murari. "A miniaturized system for imaging vascular response to deep brain stimulation." *IEEE Biomedical Circuits and Systems Conference (BioCAS),* (2013): 126-129.

[12] Luigjes, Judy, Martijn Figee, Guido van Wingen, Lukas Droge, and Wim van den Brink. "Deep Brain Stimulation Normalizes Frontostriatal Connectivity in Obsessive-Compulsive

Disorder." *BIOLOGICAL PSYCHIATRY, 360 PARK AVE SOUTH, NEW YORK, NY 10010-1710 USA: ELSEVIER SCIENCE INC,* vol. 73, no. 9 (2013): 70S-70S.

[13] Neumann, W. J., J. Huebl, C. Brücke, L. Gabriëls, M. Bajbouj, A. Merkl, G. H. Schneider, B. Nuttin, P. Brown, and A. A. Kühn. "Different patterns of local field potentials from limbic DBS targets in patients with major depressive and obsessive compulsive disorder." *Molecular Psychiatry* (2014).

[14] Figee, Martijn, Judy Luigjes, Ruud Smolders, Carlos-Eduardo Valencia-Alfonso, Guido van Wingen, Bart de Kwaasteniet, Mariska Mantione et al. "Deep brain stimulation restores frontostriatal network activity in obsessive-compulsive disorder." *Nature neuroscience,* vol. 16, no. 4 (2013): 386-387.

[15] Kuhn, J., K. Hardenacke, D. Lenartz, T. Gruendler, M. Ullsperger, C. Bartsch, J. K. Mai et al. "Deep brain stimulation of the nucleus basalis of Meynert in Alzheimer's dementia." *Molecular psychiatry* (2014).

[16] Laxton, Adrian W., and Andres M. Lozano. "Deep brain stimulation for the treatment of Alzheimer disease and dementias." *World neurosurgery,* vol. 80, no. 3 (2013): S28-e1.

[17] Visser-Vandewalle, V., L. Ackermans, C. van der Linden, Y. Temel, M. A. Tijssen, K. Schruers, P. Nederveen et al. "Deep brain stimulation in Tourette syndrome The Dutch-Flemish guidelines." *Thalamic Deep Brain Stimulation in Tourette Syndrome,* vol. 58 (2011): E590.

[18] Sprengers, Mathieu, Kristl Vonck, EVELIEN CARRETTE, Alfred Meurs, Dirk Van Roost, and Paul Boon. "A decade of experience with deep brain stimulation for patients with refractory medial temporal lobe epilepsy." *Hyper-Interaction Viability Experiments Workshop,* (2012).

[19] Hess, Christopher W., David E. Vaillancourt, and Michael S. Okun. "The temporal pattern of stimulation may be important to the mechanism of deep brain stimulation." *Experimental neurology,* vol. 247 (2013): 296-302.

[20] McIntyre, Cameron C., Marc Savasta, Lydia Kerkerian-Le Goff, and Jerrold L. Vitek. "Uncovering the mechanism (s) of action of deep brain stimulation: activation, inhibition, or both." *Clinical Neurophysiology,* vol. 115, no. 6 (2004): 1239-1248

[21] Panov, Fedor, and Brian Harris Kopell. "Use of Cortical Stimulation in Neuropathic Pain, Tinnitus, Depression, and Movement Disorders."*Neurotherapeutics* (2014): 1-8.

[22] Ostrem, J. L., G. A. Glass, L. C. Markun, C. A. Racine, M. M. Volz, S. L. Heath, and P. A. Starr. "Prospective assessment of low-versus high-frequency bilateral subthalamic nucleus (STN) deep brain stimulation (DBS) in patients with primary dystonia." *MOVEMENT DISORDERS, 111 RIVER ST, HOBOKEN 07030-5774, NJ USA: WILEY-BLACKWELL,* vol. 27 (2012): S320-S321.

[23] Bendjelid, Karim, Nicolas Schütz, Martin Stotz, Isabelle Gerard, Peter M. Suter, and Jacques-André Romand. "Transcutaneous Pco2 monitoring in critically ill adults: Clinical evaluation of a new sensor." *Critical care medicine,* vol. 33, no. 10 (2005): 2203-2206.

[24] McIntyre, Cameron C., Marc Savasta, Lydia Kerkerian-Le Goff, and Jerrold L. Vitek. "Uncovering the mechanism (s) of action of deep brain stimulation: activation, inhibition, or both." *Clinical Neurophysiology,* vol. 115, no. 6 (2004): 1239-1248.

[25] Harnack, Daniel, Wassilios Meissner, Raik Paulat, Hannes Hilgenfeld, Wolf-Dieter Müller, Christine Winter, Rudolf Morgenstern, and Andreas Kupsch. "Continuous high-frequency stimulation in freely moving rats: development of an implantable microstimulation system." *Journal of neuroscience methods,* vol. 167, no. 2 (2008): 278-291.

[26] Kussener, E., T. Barroca, B. Lincoln, P. Salin, C. Forni, O. Mainard, H. Barthelemy, and D. Goguenheim. "Integrated continuous microstimulation system for deep brain stimulation in rodent models of neurological disorders." *8th IEEE International NEWCAS Conference (NEWCAS),* (2010): 1-4.

[27] Shahrokhi, Farzaneh, Karim Abdelhalim, Demitre Serletis, Peter L. Carlen, and Roman Genov. "The 128-channel fully differential digital integrated neural recording and stimulation interface." *IEEE Transactions on Biomedical Circuits and Systems,* vol. 4, no. 3 (2010): 149-161.

[28] El Gamal, Abbas, and Helmy Eltoukhy. "CMOS image sensors." *IEEE Circuits and Devices Magazine,* vol 21, no. 3 (2005): 6-20.

[29] Morrison, S. R. "A new type of photosensitive junction device." *Solid-State Electronics*, vol. 6, no. 5 (1963): 485-494.

[30] Boyle, Willard S., and George E. Smith. "Charge coupled semiconductor devices." *Bell System Technical Journal,* vol. 49, no. 4 (1970): 587-593.

[31] Noble, Peter JW. "Self-scanned silicon image detector arrays." *IEEE Transactions on Electron Devices,* vol. 15, no. 4 (1968): 202-209.

[32] Bigas, M., Enric Cabruja, Josep Forest, and Joaquim Salvi. "Review of CMOS image sensors." *Microelectronics journal,* vol.37, no. 5 (2006): 433-451.

[33] Schneider, B., H. Fischer, S. Benthien, H. Keller, T. Lule, P. Rieve, M. Sommer, J. Schulte, and M. Bohm. "Tfa image sensors: from the one transistor cell to a locally adaptive high dynamic range sensor." *IEDM Tech. Dig.,* (1997): 209-212.[34] Weckler, Gene P. "Operation of pn junction photodetectors in a photon flux integrating mode." *IEEE Journal of Solid-State Circuits,* vol. 2, no. 3 (1967): 65-73.

[35] Lulé, Tarek, Stephan Benthien, Holger Keller, F. A. M. F. Mutze, Peter Rieve, Konstantin Seibel, Michael Sommer, and M. A. B. M. Bohm. "Sensitivity of CMOS based imagers and scaling perspectives." *IEEE Transactions on Electron Devices,* vol. 47, no. 11 (2000): 2110-2122.

[36] Fossum, Eric R. "CMOS image sensors: Electronic camera on a chip." (1995).

[37] Noble, Peter JW. "Self-scanned silicon image detector arrays." *IEEE Transactions on Electron Devices,* vol. 15, no. 4 (1968): 202-209.

[38] Wang, Xinyang, Padmakumar R. Rao, Adri Mierop, and Albert JP Theuwissen. "Random telegraph signal in CMOS image sensor pixels." *IEDM Tech. Dig.,* (2006): 1-4.

[39] Yadid-Pecht, Orly, Ran Ginosar, and Yosi Shacham-Diamand. "A random access photodiode array for intelligent image capture." *IEEE Transactions on Electron Devices,* vol. 38, no. 8 (1991): 1772-1780.

[40] Fowler, Boyd A., Janusz Balicki, Dana How, and Michael Godfrey. "Low-FPN high-gain capacitive transimpedance amplifier for low-noise cmos image sensors." *Proc. SPIE,* vol. 4306 (2011): 68.

[41] Murari, Kartikeya, Ralph Etienne-Cummings, Nitish V. Thakor, and Gert Cauwenberghs. "A CMOS in-pixel CTIA high-sensitivity fluorescence imager." *IEEE Transactions on Biomedical Circuits and Systems,* vol. 5, no. 5 (2011): 449-458.

[42] Schulz, M., and L. Caldwell. "Nonuniformity correction and correctability of infrared focal plane arrays." *Infrared Physics & Technology,* vol. 36, no. 4 (1995): 763-777.

[43] Frostig, Ron D., Edmund E. Lieke, Daniel Y. Ts'o, and Amiram Grinvald. "Cortical functional architecture and local coupling between neuronal activity and the microcirculation revealed by in vivo high-resolution optical imaging of intrinsic signals." *Proceedings of the National Academy of Sciences,* vol. 87, no. 16 (1990): 6082-6086.

[44] Licht, J. D., M. J. Grossei, J. Figge, U. M. Hansen, Y. Yokouchl, H. Sasaki, and A. Kuroiwa. "Interactions between electrical activity and cortical microcirculation revealed by imaging spectroscopy: implications for functional brain mapping." *Science,* vol. 272 (1996): 551.

[45] Vanzetta, Ivo, and Amiram Grinvald. "Increased cortical oxidative metabolism due to sensory stimulation: implications for functional brain imaging." *Science,* vol. 286, no. 5444 (1999): 1555-1558.

[46] Nemoto, Masahito, Yasutomo Nomura, Chie Sato, Mamoru Tamura, Kiyohiro Houkin, Izumi Koyanagi, and Hiroshi Abe. "Analysis of optical signals evoked by peripheral nerve

stimulation in rat somatosensory cortex: dynamic changes in hemoglobin concentration and oxygenation." *Journal of Cerebral Blood Flow & Metabolism*, vol. 19, no. 3 (1999): 246-259.

[47] Weber, Bruno, and Fritjof Helmchen, eds. *Optical Imaging of Neocortical Dynamics*. Humana Press, 2014.

[48] Villringer, Arno, and Britton Chance. "Non-invasive optical spectroscopy and imaging of human brain function." *Trends in neurosciences*, vol. 20, no. 10 (1997): 435-442.

[49] Lambert, Johann Heinrich. *Lamberts Photometrie:(Photometria, sive De mensura et gradibus luminis, colorum et umbrae)(1760)*. No. 31-33. W. Engelmann, 1892

[50] Lulé, Tarek, Stephan Benthien, Holger Keller, F. A. M. F. Mutze, Peter Rieve, Konstantin Seibel, Michael Sommer, and M. A. B. M. Bohm. "Sensitivity of CMOS based imagers and scaling perspectives." *IEEE Transactions on Electron Devices*, vol. 47, no. 11 (2000): 2110-2122.

[51] Lee, Dongmyung, Kunhee Cho, Dongsoo Kim, and Gunhee Han. "Low-noise in-pixel comparing active pixel sensor using column-level single-slope ADC." *IEEE Transactions on Electron Devices*, vol. 55, no. 12 (2008): 3383-3388.

[52] Ay, Suat U. "A CMOS energy harvesting and imaging (EHI) active pixel sensor (APS) imager for retinal prosthesis." *IEEE Transactions on Biomedical Circuits and Systems*, vol. 5, no. 6 (2011): 535-545.

[53] Lim, Seunghyun, Jimin Cheon, Youngcheol Chae, Wunki Jung, Dong-Hun Lee, Minho Kwon, Kwisung Yoo, Seogheon Ham, and Gunhee Han. "A 240-frames/s 2.1-Mpixel CMOS

image sensor with column-shared cyclic ADCs." *IEEE Journal of Solid-State Circuits,* vol. 46, no. 9 (2011): 2073-2083.

[54] Park, Joon Hyuk, Jelena Platisa, Vincent Pieribone, and Eugenio Culurciello. "A second-generation imaging system for freely moving animals." *IEEE International Symposium on Circuits and Systems (ISCAS),* (2012): 105-108.

[55] Seo, Min-Woong, Sung-Ho Suh, Tetsuya Iida, Taishi Takasawa, Keigo Isobe, Takashi Watanabe, Shinya Itoh, Keita Yasutomi, and Shoji Kawahito. "A low-noise high intrascene dynamic range CMOS image sensor with a 13 to 19b variable-resolution column-parallel folding-integration/cyclic ADC." *IEEE Journal of Solid-State Circuits,* vol. 47, no. 1 (2012): 272-283.

[56] Eltoukhy, Helmy, Khaled Salama, and Abbas El Gamal. "A 0.18-μm CMOS bioluminescence detection lab-on-chip." *IEEE Journal of Solid-State Circuits,* vol. 41, no. 3 (2006): 651-662.

[57] Furuta, Masanori, Yukinari Nishikawa, Toru Inoue, and Shoji Kawahito. "A high-speed, high-sensitivity digital CMOS image sensor with a global shutter and 12-bit column-parallel cyclic A/D converters." *IEEE Journal of Solid-State Circuits,* vol. 42, no. 4 (2007): 766-774.

[58] Xu, Ruoyu, Bing Liu, and Jie Yuan. "A 1500 fps highly sensitive 256 256 CMOS imaging sensor with in-pixel calibration." *IEEE Journal of Solid-State Circuits,* vol. 47, no. 6 (2012): 1408-1418.

[59] Nixon, Robert H., Sabrina E. Kemeny, Craig O. Staller, and Eric R. Fossum. "128 x 128 CMOS photodiode-type active pixel sensor with on-chip timing, control, and signal chain electronics." *International Society for Optics and Photonics in IS&T/SPIE's Symposium on Electronic Imaging: Science & Technology*, (1995): 117-123.